Transitory microbial habitat in the hyperarid Atacama Desert

Dirk Schulze-Makuch[a,b,1], Dirk Wagner[c,d], Samuel P. Kounaves[e,f], Kai Mangelsdorf[g], Kevin G. Devine[h], Jean-Pierre de Vera[i], Philippe Schmitt-Kopplin[j,k], Hans-Peter Grossart[l,m], Victor Parro[n], Martin Kaupenjohann[o], Albert Galy[p], Beate Schneider[a,c], Alessandro Airo[a], Jan Frösler[q], Alfonso F. Davila[r], Felix L. Arens[s], Luis Cáceres[t], Francisco Solís Cornejo[t], Daniel Carrizo[n], Lewis Dartnell[u], Jocelyne DiRuggiero[v], Markus Flury[w], Lars Ganzert[l], Mark O. Gessner[l,x], Peter Grathwohl[y], Lisa Guan[z], Jacob Heinz[a], Matthias Hess[aa], Frank Keppler[bb], Deborah Maus[a], Christopher P. McKay[r], Rainer U. Meckenstock[q], Wren Montgomery[f], Elizabeth A. Oberlin[e], Alexander J. Probst[q], Johan S. Sáenz[z], Tobias Sattler[bb], Janosch Schirmack[a], Mark A. Sephton[f], Michael Schloter[z,cc], Jenny Uhl[k], Bernardita Valenzuela[t], Gisle Vestergaard[z], Lars Wörmer[dd], and Pedro Zamorano[t]

[a]Center of Astronomy & Astrophysics, Technical University Berlin, 10623 Berlin, Germany; [b]School of the Environment, Washington State University, Pullman, WA 99164; [c]Section Geomicrobiology, GFZ German Research Centre for Geosciences, 14473 Potsdam, Germany; [d]Institute of Earth and Environmental Science, University of Potsdam, 14476 Potsdam, Germany; [e]Department of Chemistry, Tufts University, Medford, MA 02153; [f]Department of Earth Science & Engineering, Imperial College London, London SW72AZ, United Kingdom; [g]Section Organic Geochemistry, GFZ German Research Centre for Geosciences, 14473 Potsdam, Germany; [h]School of Human Sciences, London Metropolitan University, London N7 8BD, United Kingdom; [i]Astrobiological Laboratories, Management and Infrastructure, Institute for Planetary Research, German Aerospace Center, 12489 Berlin, Germany; [j]Analytical Food Chemistry, Technical University München, 85354 Freising-Weihenstephan, Germany; [k]Analytical BioGeoChemistry, Helmholtz Zentrum München, 85764 Oberschleissheim, Germany; [l]Department of Experimental Limnology, Leibniz Institute of Freshwater Ecology and Inland Fisheries, 16775 Stechlin, Germany; [m]Institute of Biochemistry & Biology, University of Potsdam, 14476 Potsdam, Germany; [n]Molecular Evolution Department, Centro de Astrobiología, Instituto Nacional de Técnica Aeroespacial-Consejo Superior de Investigaciones Científicas (INTA-CSIC), 28850 Madrid, Spain; [o]Fachgebiet Bodenkunde, Technical University Berlin, 10623 Berlin, Germany; [p]Centre de Recherches Pétrographiques et Géochimiques, CNRS, Université de Lorraine, 54500 Vandoeuvre les Nancy, France; [q]Biofilm Centre, University of Duisburg-Essen, 45141 Essen, Germany; [r]Planetary Systems Branch (Code SST), NASA Ames Research Center, Moffett Field, CA 94035; [s]Institute for Geological Sciences, Freie University Berlin, 12249 Berlin, Germany; [t]Laboratorio de Microorganismos Extremófilos, University of Antofagasta, Antofagasta 02800, Chile; [u]Department of Life Sciences, University of Westminster, London W1W 6UW, United Kingdom; [v]Department of Biology, The John Hopkins University, Baltimore, MD 21218; [w]Department of Crop & Soil Sciences, Washington State University, Pullman, WA 99164; [x]Department of Ecology, Technical University Berlin, 10587 Berlin, Germany; [y]Center for Applied Geosciences, University of Tübingen, 72074 Tübingen, Germany; [z]Comparative Microbiome Analysis, Helmholtz Zentrum München, 85764 Oberschleissheim, Germany; [aa]Systems Microbiology & Natural Products Laboratory, University of California, Davis, CA 95616; [bb]Institute of Earth Sciences, Heidelberg University, 69120 Heidelberg, Germany; [cc]Soil Science, Technical University München, 85354 Freising-Weihenstephan, Germany; and [dd]Center for Marine Environmental Sciences (MARUM), University of Bremen, 28359 Bremen, Germany

Edited by Mary K. Firestone, University of California, Berkeley, CA, and approved January 25, 2018 (received for review August 17, 2017)

Traces of life are nearly ubiquitous on Earth. However, a central unresolved question is whether these traces always indicate an active microbial community or whether, in extreme environments, such as hyperarid deserts, they instead reflect just dormant or dead cells. Although microbial biomass and diversity decrease with increasing aridity in the Atacama Desert, we provide multiple lines of evidence for the presence of an at times metabolically active, microbial community in one of the driest places on Earth. We base this observation on four major lines of evidence: (*i*) a physico-chemical characterization of the soil habitability after an exceptional rain event, (*ii*) identified biomolecules indicative of potentially active cells [e.g., presence of ATP, phospholipid fatty acids (PLFAs), metabolites, and enzymatic activity], (*iii*) measurements of in situ replication rates of genomes of uncultivated bacteria reconstructed from selected samples, and (*iv*) microbial community patterns specific to soil parameters and depths. We infer that the microbial populations have undergone selection and adaptation in response to their specific soil microenvironment and in particular to the degree of aridity. Collectively, our results highlight that even the hyperarid Atacama Desert can provide a habitable environment for microorganisms that allows them to become metabolically active following an episodic increase in moisture and that once it decreases, so does the activity of the microbiota. These results have implications for the prospect of life on other planets such as Mars, which has transitioned from an earlier wetter environment to today's extreme hyperaridity.

habitat | aridity | microbial activity | biomarker | Mars

Significance

It has remained an unresolved question whether microorganisms recovered from the most arid environments on Earth are thriving under such extreme conditions or are just dead or dying vestiges of viable cells fortuitously deposited by atmospheric processes. Based on multiple lines of evidence, we show that indigenous microbial communities are present and temporally active even in the hyperarid soils of the Atacama Desert (Chile). Following extremely rare precipitation events in the driest parts of this desert, where rainfall often occurs only once per decade, we were able to detect episodic incidences of biological activity. Our findings expand the range of hyperarid environments temporarily habitable for terrestrial life, which by extension also applies to other planetary bodies like Mars.

The core region of the Atacama Desert is the most arid midlatitude desert on Earth and in the past has been devoid of precipitation for decades. A mean annual precipitation of <20 mm reduces weathering rates and leaching losses to levels below the accumulation rates of atmospheric salts and dust (1). Hence,

Author contributions: D.S.-M. designed research; D.S.-M., D.W., S.P.K., K.M., K.G.D., J.-P.d.V., P.S.-K., H.-P.G., V.P., A.G., B.S., A.A., J.F., A.F.D., F.L.A., L.C., F.S.C., D.C., L.D., J.D., M.F., L. Ganzert, M.O.G., P.G., L. Guan, J.H., M.H., F.K., D.M., R.U.M., W.M., E.A.O., A.J.P., J.S.S., T.S., J.S., M.A.S., M.S., J.U., B.V., G.V., L.W., and P.Z. performed research; D.W., S.P.K., K.M., K.G.D., P.S.-K., H.-P.G., V.P., M.K., A.G., M.O.G., P.G., F.K., R.U.M., A.J.P., M.S., G.V., and L.W. contributed new reagents/analytic tools; D.S.-M., D.W., S.P.K., K.M., K.G.D., J.-P.d.V., P.S.-K., H.-P.G., V.P., M.K., A.G., B.S., A.A., J.F., A.F.D., F.L.A., L.D., J.D., M.F., L. Ganzert, M.O.G., P.G., M.H., F.K., C.P.M., R.U.M., A.J.P., J.S., M.S., J.U., B.V., G.V., and L.W. analyzed data; and D.S.-M., D.W., S.P.K., H.-P.G., and M.S. wrote the paper.

The authors declare no conflict of interest.

This article is a PNAS Direct Submission.

Data deposition: The metagenome sequences reported in this paper have been deposited in the EMBL-EBI database (accession no. PRJEB20402 with the sample IDs ERS1666624–ERS1666714) and in the GenBank/EMBL database (BioProject ID PRJNA395196).

[1]To whom correspondence should be addressed. Email: schulze-makuch@tu-berlin.de.

This article contains supporting information online at www.pnas.org/lookup/suppl/doi:10.1073/pnas.1714341115/-/DCSupplemental.

atmospheric deposition over millions of years has resulted in high salt concentrations in the soils of the hyperarid area (2). The only documented microhabitats in the core region of the Atacama Desert are colonized by microbial communities thriving in surficial salt crusts, where microbial activity is enabled through deliquescence (3, 4). Even though there are traces of microbial life in the subsurface of the Atacama Desert (5), it remains unclear whether these environments support active microbial growth or whether the observed cells are sporadically introduced by atmospheric transport and continuously inactivated and degraded. To answer this question, in April of 2015 we sampled soils from the surface and near subsurface at six locations along a decreasing moisture gradient [coastal soil (CS), alluvial fan (AL), red sands (RS), Maria Elena (ME), Yungay (YU), and Lomas Bayas (LB)] (*SI Appendix*, Fig. S1) and characterized them and their microbial communities by using a broad suite of complementary methods. Since this sampling occurred shortly after an unexpected rain event, we repeated sampling in February 2016 and January 2017 to determine whether the detected microbial activity in 2015 was ongoing or episodic and related to the temporary increased availability of moisture.

Results

Environmental Setting. The selected CS site has been occasionally subject to fog and rain, while sites further inland (ME, YU, and LB) are located in hyperarid areas (6, 7), where water content of surface soils is generally <1% by weight (*SI Appendix*, Fig. S2). Water activity is often below the threshold of ∼0.6 required to sustain metabolic activity (8). Relative humidity levels are generally below 30% and daily UV irradiation doses were ca. 30 $J{\cdot}m^{-2}$. Except for LB, where total organic carbon (TOC) reached 0.25% (wt/wt), TOC at all other sites was less than 0.1%. A prerequisite of our study was that the sampled sites are relatively pristine and little affected by human contamination, which was the case based on measured polycyclic aromatic hydrocarbon concentrations which are extremely low and generally in the microgram per kilogram range or lower. Soil minerals at all sites are dominated by alkali feldspar and plagioclase with minor amounts of quartz, chlorite, and amphibole, with some sites displaying a significant amount of anhydrite, bassanite, gypsum, and carbonates. Sites subject to higher levels of moisture (CS, AL, RS) contain large amounts of chlorides (e.g., halite), while soils obtained from the hyperarid areas (YU, ME, LB) mostly contain sulfates (e.g., gypsum or anhydrite), perchlorates (ClO_4^-), and chlorates (ClO_3^-) (*SI Appendix*, Fig. S3). The first set of field samples was taken in April 2015 1 mo after a major El Niño triggered one of the rare rainfall events in the Atacama Desert (9). Eight millimeters of precipitation was recorded at Baquedana and 33 mm at Antofagasta, which was the highest amount of precipitation since the beginning of the official recording in 1978 (*SI Appendix*, Fig. S2*C*) and affected all study sites. The second and third sampling campaigns were conducted in February 2016 and January 2017, respectively, with only two minor rain events in between (each 6.7 mm, recorded at Antofagasta).

Microbial Diversity. Metagenomic analyses of the DNA pool from topsoils revealed a high bacterial diversity at CS (nonpareil diversity index of 21.2 ± 0.5), similar to sandy soils, but considerably higher compared with the drier areas of YU and ME (nonpareil indexes of 19.5 ± 0.6 and 18.9 ± 0.1, respectively; *SI Appendix*, Fig. S4*A*). Phylogenetic profiles (*SI Appendix*, Fig. S4*B*) indicate that soils at YU were associated with microbiomes typical for sandy environments and desert soils, mainly consisting of *Actinobacteria* (5) with *Corynebacteriales*, *Streptomycetales*, and *Micrococcales* being the dominant suborders and a proportional decline of *Rubrobacterales* from the surface to the subsurface. In contrast, ME was dominated by *Geodermatophilaceae*, known to colonize hyperarid habitats (10) and tolerate high levels of oxidative stress, desiccation, salts, and metals (11). The same general trend of decreased biomass and diversity with increasing aridity was found for *Archaea* and *Fungi*, even though their proportion was lower than that of *Bacteria*. In all soil samples ∼200 fungal marker genes were detected, almost exclusively belonging to *Ascomycota* and *Basidiomycota* (*SI Appendix*, Fig. S5 *A* and *B*). At CS, *Archaea* (mainly halobacteria) reached a maximum and dominated the microbial community at a depth of 20–30 cm, while everywhere else they accounted for <4% of sequence reads (*SI Appendix*, Fig. S5*C*). Our DNA-based data were corroborated by phospholipid fatty acid profiles (Fig. 1 *B* and *D*), serving as biomarkers for living bacteria (12), and cultivation-based approaches both identifying *Actinobacteria* (e.g., *Actinobacterium lienomycini*, *Kocuria* sp., *Pseudonocardina* sp., *Streptomyces* sp.), *Proteobacteria* (e.g., *Pseudomonas* sp., *Paracoccus marinus*), and *Firmicutes* (e.g., *Bacillus litoralis*, *Bacillus simplex*, *Halobacillus* sp.).

Abundance and Identification of Dead and Living Microorganisms. A unique cell-separation technique (13) was used to differentiate between intracellular DNA (iDNA) indicating physically intact and potentially viable cells and extracellular DNA (eDNA) mainly representing preserved DNA from dead cells.

Quantitative PCR (qPCR) using universal bacterial primers was performed for both DNA pools, for all soil samples taken along the moisture gradients in 2015 and 2017, and at YU in 2016. After the rain event in 2015, the abundance of 16S rRNA genes in the iDNA pool (proxy of living bacterial biomass) was generally higher than in 2016/2017 (between $\sim10^3$ and $\sim10^6$ gene copies per gram soil; *SI Appendix*, Table S1), increasing with moisture (*SI Appendix*, Fig. S6). The copy numbers in the eDNA pool showed larger variations of between $\sim10^1$ and $\sim10^7$ gene copies per gram soil, and only at LB was no eDNA detectable with the primers applied in the qPCR. In contrast to the relatively high gene copy numbers in 2015, soil samples from the same sites, but taken 2 y after the rain event, revealed a drastic decrease in living cells (iDNA; equal to or less than 10^2 gene

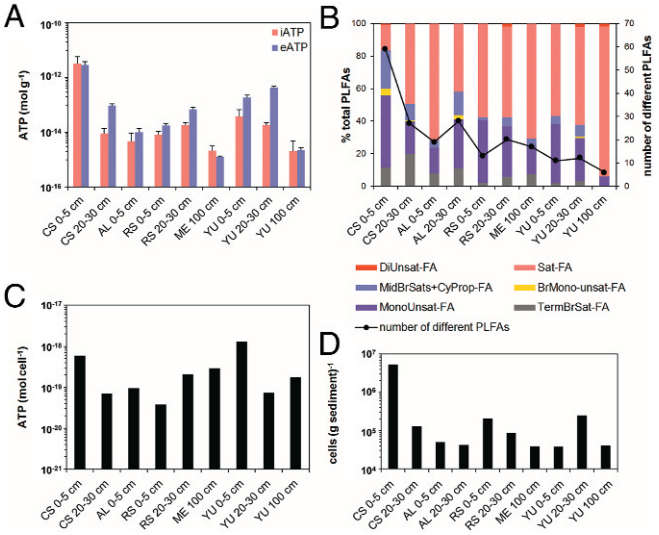

Fig. 1. (*A* and *B*) Concentrations of intracellular ATP (iATP) and extracellular ATP (eATP) (both n = 3) (*A*) and PLFAs (*B*) in Atacama Desert soils. A decrease in the number of identified PLFAs indicates a decrease in diversity, which is related to increasing aridity. (*C* and *D*) Average cell-based ATP concentrations were obtained by relating iATP concentrations (*C*) to total biomass levels (*D*) measured at specific locations, which were obtained from PLFA analysis.

copies per gram soil). The same trend was also visible in the eDNA pool although gene copy numbers were somewhat higher than in the iDNA pool (*SI Appendix*, Table S1).

To provide a detailed characterization of living and dead microorganisms, high-throughput sequencing of 16S rRNA gene amplicons of both DNA pools was performed. In environments supporting an active microbial community, the eDNA pool is continuously replenished through biomass turnover of living cells (14). As indicated by the large number of shared operational taxonomic units (OTUs), this was likely the case at CS where relative humidity (RH) and nutrients were highest, constantly supplied by coastal fog. In contrast, OTUs identified at the hyperarid locations showed less overlap between eDNA and iDNA compared with CS, suggesting the dominance of autochthonous microbial taxa rather than of inactive transitory microorganisms periodically introduced by wind (Fig. 2*A*). Key organisms of these communities consisted of unclassified *Acidimicrobiales*, *Actinobacteria*, *Alicyclobacillus*, *Burkholderia*, *Comamonadaceae*, and *Xanthomonadaceae*. Although abundances differed among sites and soil depths, these characteristic taxa identified from iDNA were found in all samples from all sites and depths, suggesting a native and metabolically active desert core community.

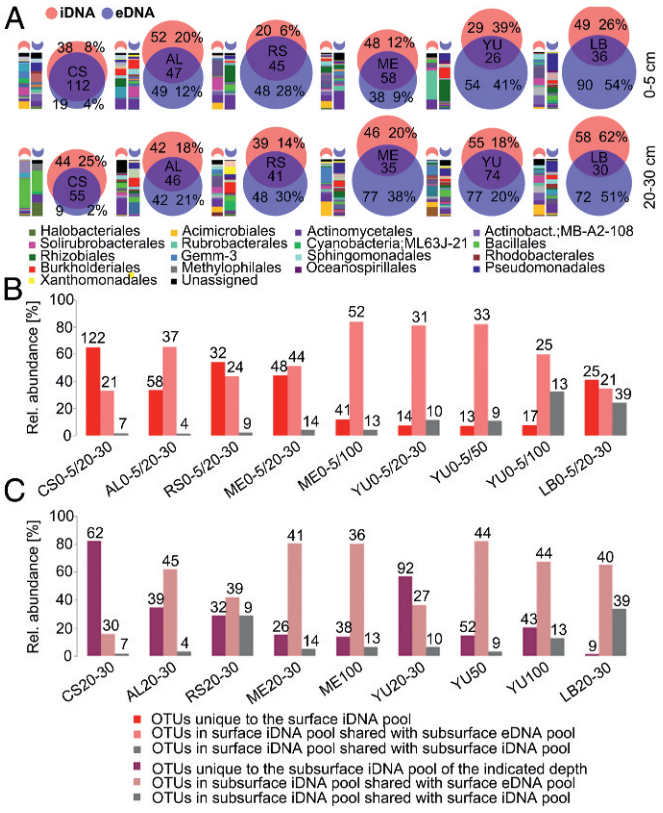

Fig. 2. Microbial community structure and relationship between iDNA and eDNA pools at six soil sampling sites in the Atacama Desert: CS, AL, RS, ME, YU, and LB. (*A*) Venn diagrams of iDNA and eDNA OTU intersections for samples collected at 0–5 cm and 20–30 cm depth. Numbers indicate the numbers of different OTUs, and percentages refer to relative abundances of reads unique to iDNA or eDNA. Bars to the left of the Venn diagrams show relative abundances of bacterial orders in the subsets unique to the iDNA and eDNA pools of the indicated sampling depth. (*B*) Classification of iDNA pools from soil surface samples (0–5 cm) collected at the six sampling sites in comparison with the iDNA and eDNA pools in subsurface soil layers. (*C*) Classification of the subsurface iDNA pools (20–30 cm, 50 cm, 100 cm) in comparison with the iDNA and eDNA pools in the surface soils (0–5 cm). The bars show the percentages of OTU reads in the corresponding subsets, and numbers indicate the numbers of different OTUs.

In general, as dryness increased, microbial diversity decreased, analogous to previous observations (15, 16).

Abundance of Endospores. The dormant component of the bacterial communities was specifically assessed for the 2015 sampling period by quantifying endospores, which are characteristic of the phylum *Firmicutes* and stand out by their exceptional resistance to environmental stresses. Dipicolinic acid (DPA), a specific biomarker of intact endospores, was detected at all sites. Endospore concentrations in surface layers, however, decreased with increasing aridity by almost two orders of magnitude (7.7×10^5 to 1.5×10^4 spores per gram soil; *SI Appendix*, Table S2). The large size of this community suggests that an extensive and persistent *Firmicutes* seed bank remains available in the Atacama Desert, which is in agreement with the dominance of isolates from this phylum in our cultivation experiments. Importantly, the contribution of endospores to the iDNA pool was likely minor, because the conventional extraction methods that were used to extract iDNA from intact cells do not usually extract DNA from spores (17). Therefore, it is not surprising that the phylogenetic composition derived from iDNA sequencing does not reflect the abundance of endospores from the phylum *Firmicutes* (*SI Appendix*, Fig. S7).

Metabolic Activity. As many of the cultivated bacteria were spore formers, we used independent complementary analytical approaches to obtain conclusive evidence for living microorganisms and their potential activity in hyperarid habitats.

First, evidence for microbial activity was obtained by a fluorescein diacetate hydrolysis assay to determine enzymatic activity (*SI Appendix*, Table S3). Enzymatic activity was highest at the surface of CS, ME, and LB sites, but still detectable at all other sites and shallow depths (0–5 cm and 20–30 cm, respectively), except for LB 20–30 cm, where it was below the detection limit of 10^{-3} nmol·g^{-1}·h^{-1}.

Second, our hypothesis of active, native microbial communities was supported by ATP analyses. These analyses allow the separation of intracellular ATP (iATP), indicative of viable cells, and extracellular ATP (eATP), indicative of ATP remaining in the soil after cell lysis. iATP levels were up to three orders of magnitude higher (3×10^{-12} mol·g^{-1}) at CS compared with the sampling sites located in the driest desert core (e.g., 2×10^{-15} mol·g^{-1} at YU 100 cm depth; Fig. 1). Overall, ATP analyses supported the general trend of decreasing microbial activity with increasing aridity, both along the studied moisture transect (2015) and in YU surface soils from 2015 to 2017 (*SI Appendix*, Table S1). The ATP analyses provide evidence that even in the most arid sites of the Atacama core region native microorganisms can be at times metabolically active.

Third, the presence of metabolically active microorganisms was supported by the analyses of water-extractable metabolites via direct injection electrospray ionization Fourier-transform ion cyclotron resonance mass spectrometry [ESI(-) FT-ICR-MS], which allowed the accurate calculation of elemental formulas. On average, a rich signature of ~1,600 elemental compositions (CHNOS) was detected in all samples, indicating a geochemical footprint (18) typical of natural organic matter superimposed by a biological footprint of fresh organic material (19) involving amino acids, small peptides, and fatty acids (*SI Appendix*, Fig. S8). Results suggest that water-soluble organic compounds consisted mainly of aliphatic carbohydrates and fatty acids (CHO), while nitrogen- and sulfur-containing compounds (CHNO and CHOS) were less abundant. The relative abundance of compounds, predominantly reflecting metabolic activity, decreased significantly along the aridity gradient from the coast to inland with constant low amounts of organic compounds at the hyperarid locations of ME, YU, and LB. This trend again suggests a marked decline in metabolic activity from moist to hyperarid soil habitats

(*SI Appendix*, Fig. S9). Nevertheless, there was clear conservation of biosignatures even in the hyperarid locations, showing evidence of past and, most likely, recent metabolic activity, especially at a depth of 20–30 cm in YU (2015), where different types of metabolites were distinguishable (*SI Appendix*, Fig. S9*F*).

Fourth, the metagenomic analysis from the soil samples obtained in April 2015 indicated that microorganisms were active even in the driest soil samples. Sequence abundance of mycobacteriophages, gordoniaphages, and streptomycophages correlated positively with that of their respective hosts found in the different samples [Spearman coefficient correlations of $\rho = 0.69$ at CS, $\rho = 0.88$ at ME, and $\rho = 0.67$ at YU (*SI Appendix*, Fig. S4 *C*–*E*)]. The detected virus–host relationships seem to be consistent with the observations that microbial blooms are followed by a bloom of phages specific for the microbes that dominated the microbial bloom (20, 21). However, while most identified viruses are phages persistent in the environment that have also been identified by other desert studies (22), the vast majority of the identified viruses (95+%) belong to the family Caudovirales, which includes both virulent and temperate members. Thus, we cannot exclude the presence of a large number of undetected prophages that might stay dormant for long periods of time.

Finally, we investigated in situ genome replication rates of organisms via a genome-resolved metagenomics approach (23) of samples retrieved from YU and ME. For YU, we reconstructed a draft genome of the most dominant organism (uncultivated *Actinobacteria*) with an estimated completeness of 92% based on single-copy genes (Fig. 3). The iRep value (24) of the genome was 1.57, which is indicative of its slow replication. For the ME site, we retrieved three high-quality draft genomes belonging to members of the phyla *Chloroflexi*, *Actinobacteria*, and *Saccharibacteria* (completeness 86–98%; Fig. 3). The in situ replication rates of these genomes varied between 1.86 and 3.31. The lower replication rates compare with literature values of a wide array of organisms across multiple phyla, but the iRep value of 2.48 for the *Chloroflexi* indicates that each genome in the population has on average one bidirectional replication ongoing (24). The genome replication rate for the *Actinobacteria* was extremely high, which indicates that each genome of this population had several replication forks at the time of sampling, thus providing strong evidence for microbial activity.

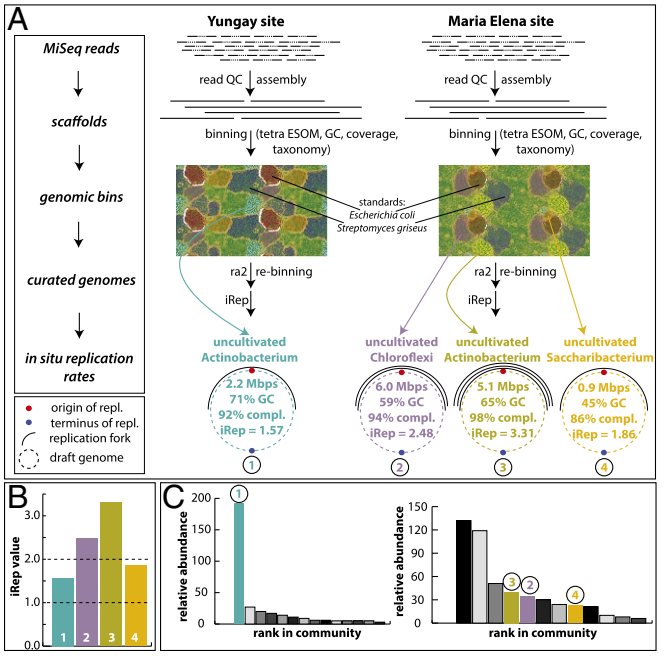

Fig. 3. Genome-resolved metagenomics analyses and results. (*A*) Work flow and main results from genome-resolved metagenomics. For details please see *SI Appendix*, *Read-Based Metagenomics, Genome-Resolved Metagenomics and in Situ Replication Rates*. Genome replication forks are symbolic. (*B*) Overview of iRep values retrieved from the four genomes from the YU and ME sites (color codes correspond to those in *A*). Dashed line at value 1 marks threshold at which no replication occurs. Dashed line at value 2 marks where each genome of a population has on average bidirectional replication taking place (24). (*C*) Rank-abundance curves based on rpS3 genes. Colored genomes correspond to those in *A* and *B*. For the YU site (*Left* rank-abundance curve) the most dominant organism was reconstructed, and all other genomes were fragmented. For the ME site (*Right* rank-abundance curve) three genomes were reconstructed. The three most abundant organisms were *Actinobacteria*, which were similar in GC and abundance.

A Transitory Habitat? The continuous decline of nonstructural water at 20–30 cm depth at YU, from 2.7% by weight in 2015 to 0.2% and 0.1% in 2016 and 2017, respectively, suggests temporarily favorable conditions for the activity of specialized microorganisms after the rare precipitation event until water activity fell again beneath a critical threshold (Fig. 4*A*). Mineralogical data confirmed a desiccation process in the later years as some of the gypsum at YU 20–30 cm dehydrated to anhydrite (Fig. 4*B*). The steep decline of recovered iDNA by three to five orders of magnitudes (Fig. 4 *C* and *D*) indicates that the sampling campaign in 2015, shortly after a major and very rare rainfall event, tapped into a temporary, time-constrained habitat, rather than a permanent one. ATP analyses, indicative of active organisms, also support that assessment. The iATP values follow that trend, declining by more than three orders of magnitude in the YU surface soil (Fig. 4*E*), but remain constant in the deeper soil layer at YU (Fig. 4*F*), pointing to a longer retention of microbial activity. Possibly some water released by the desiccation of gypsum to anhydrite remains accessible to a specific part of the microbial community. This possibility is supported by isotopic evidence. The δD values for the waters in the hydrous sulfate minerals suggest that small amounts of water accessible to microorganisms might be available even in these hyperarid soils (*SI Appendix*, Table S4), e.g., in the form of thin H_2O films at mineral surfaces (25) or as a product of mineral–water exchange reactions (26).

Two other rainfall events occurred in August 2015 and June 2016 (each 6.7 mm at Antofagasta), but it is unclear how much rain fell at YU. No indication of that rainfall event was observed in our sharply declining iDNA and iATP values for the surface soils from April 2015 to January 2017. This suggests that both the August 2015 and June 2016 events were either insufficient to trigger temporarily habitable conditions and a microbial response or, since they occurred several months before our next sampling round, were too small and subsided by the time we resampled. Davis et al. (27) estimated that 2 mm or more precipitation are needed to provide free water for the support of biological activity in the soil. In previous studies, Navarro-Gonzalez et al. (7) were not able to recover any DNA from the YU site, and Warren-Rhodes et al. (28) reported on the virtual absence of hypolithic cyanobacteria. Certainly, the literature data can provide only a qualitative assessment about the presence or activity of microorganisms, because of both the methodologies used and the spatial heterogeneity of the sites. In contrast to our study, it appears that previous sampling campaigns did not tap into habitable conditions.

Discussion

The Atacama Desert soil microbiome has evolved as a result of the prevailing environmental conditions. While the soil surface was dominated by desiccation and UV-resistant species (*Geodermatophilaceae* and *Rubrobacter*), deeper layers with higher salt content were dominated by halophilic bacteria such as

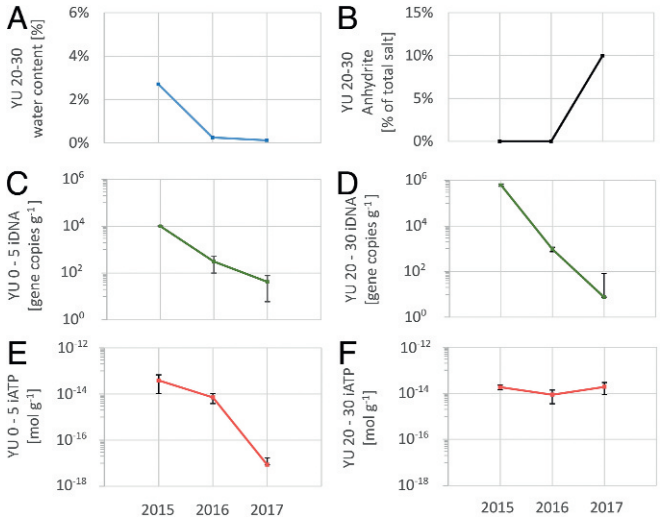

Fig. 4. Comparison of sampling events of April 2015, February 2016, and January 2017 at YU. (*A*) Available nonstructural water decreases significantly from 2015 to 2017. (*B*) Some of the gypsum at YU 20–30 desiccated and formed anhydrite. (*C* and *D*) Intracellular DNA amounts indicative of living organisms drop by several orders of magnitudes at 0–5 cm and 20–30 cm depths. (*E* and *F*) Intracellular ATP amounts indicative of active organisms drop by several orders of magnitudes at 0–5 cm, but stay constant at 20–30 cm depth.

Betaproteobacteria (*Comamonadaceae*) or *Firmicutes* (*Bacillaceae*, *Alicyclobacillaceae*) (*SI Appendix*, Fig. S7) and halophilic *Archaea* (i.e., *Halobacteria*) at CS 20–30 cm (*SI Appendix*, Fig. S5*C*). Notably, microbiomes associated with the hyperarid soils were dominated by *Bacteria* rather than *Archaea*, consistent with an assessment of the global distribution of archaeal abundances in soils (29). The amount of unique OTUs in the iDNA pool of the surface and subsurface soils of the hyperarid localities ME and YU was much lower than at the moister sites. OTUs shared between iDNA recovered from the surface and eDNA from deeper layers (Fig. 2*B*) and between iDNA from the subsurface and eDNA from the surface (Fig. 2*C*) drastically increased compared with those in CS, indicating distinct microbial populations at different depths with increasing dryness. This indicates that selection pressures for microorganisms were much higher in the hyperarid surface soils than in the wetter coastal area, resulting in species well adapted to the extreme dryness and UV radiation. However, some salt-tolerant bacteria such as *Acidimicrobiales*, *Comamonadaceae*, and *Bacillaceae* potentially survive in deeper soil layers after being buried (*SI Appendix*, Fig. S7), e.g., by ongoing atmospheric deposition of salts and sediments or by halo- and thermoturbation of soils. Alternatively, microbial communities might have persisted in the subsurface since the onset of desertification, or an initial community successively changed over geological time to cope with altered environmental conditions (5). Our results suggest that incoming microbial "newcomers" have at least been exposed to passive environmental selection, but also maintain transient activity even in the deeper soil layers and sustain viability in the Atacama Desert for very long time periods. However, it remains questionable whether the organisms found in this environment are adapting to the harsh conditions present. Bacteria reaching the Atacama Desert by atmospheric processes have been exposed to desiccation and UV stress during aerial transport, possibly for extended periods (30). This suggests that environmental species filtering could be an important factor contributing to shaping the indigenous microbial communities. In line with this hypothesis, our shotgun metagenomics data revealed several genes associated with dehydration tolerance [e.g., *groEL*, *dnaK*, *fadD*, *glgX-malZ*, *phaC* (31)] and radiation/desiccation tolerance [e.g., recQ (32)]. Immunoassays corroborated these metagenomic results by detecting ATP synthase, GroEL, CspA, and DPS DNA-protecting proteins at YU (50 cm), CS, and RS, and metaproteomic analyses of samples taken at YU also confirmed the presence of ATP synthase and GroEL.

One additional challenge for microorganisms to persist at both surface and subsurface locations is the low organic matter content characteristic of hyperarid soils. A higher TOC and moisture content allowed a higher total microbial biomass and diversity (Fig. 1 and *SI Appendix*, Fig. S6). For example, chloromethane (CH_3Cl) release during low-temperature thermolysis of surface soil samples, which is indicative of heteroatom-bonded methyl groups of organic matter, was highest for CS ($\sim$300 ng·g^{-1}) and much lower at the hyperarid sites ($\sim$1–5 ng·g^{-1}) (*SI Appendix*, Fig. S10). Stable hydrogen isotope analyses of the released chloromethane confirmed the biochemical origin of the methyl group. The emission profiles of CH_3Cl are almost identical to observations made by the Curiosity rover on Mars (33), where even harsher environmental conditions prevail than in the hyperarid core of the Atacama Desert [lack of water, scarcity of organic matter, high UV irradiation, and high salt content in the soils including bassanite and perchlorates (34)]. No rain can fall from the Martian atmosphere today (35), but liquid water can be present near the Martian surface in the form of nightly snow storms/ice microbursts (36), fog (37), near-surface groundwater (38), and possibly also from mineral dehydration reactions (39). On Mars, the deeper soil layers with a higher water activity and reduced exposure to environmental stresses (e.g., UV irradiation, large daily temperature fluctuations) are expected to be more suitable for supporting life. At YU this was the case, with the gypsum-rich soil layer at a depth of 20–30 cm containing a higher biomass and microbial diversity (Figs. 1 *B* and *D* and 2) and also retaining a similar level of activity beyond 2015 for at least 2 y more. Thus, we observe in the hyperarid core of the Atacama Desert a transitory habitat with microorganisms that are active for short periods of time and which can serve as a reasonable working model for Mars.

Conclusions

Although both microbial biomass and diversity in the Atacama Desert decrease with increasing aridity, our study shows that even the lowest precipitation levels on Earth can sustain episodic incidences of microbial activity. There is no single agreed-upon method known to date reaching the bar of evidence for microbial activity for such low-biomass environments. However, using our complementary tool box of combining different methodologies, including unique genome-resolved metagenomics, we have addressed the question of microbial activity and can answer it positively for the sampling time after the major precipitation event in 2015. Thereafter, the biomarkers for microbial activity dropped dramatically, inferring that the transitory habitable conditions have ended until the next major rain event may occur, providing a sufficient amount of free water for the microbial biota. The insights gained from the hyperarid core of the Atacama Desert can serve as a working model for Mars, where environmental stresses are even harsher. If life ever evolved on Mars, the results presented here suggest that it could have endured the transition from the early aquatic stage, through increasing aridity cycles, and perhaps even found a subsurface niche beneath today's severely hyperarid surface.

Materials and Methods

Detailed methods, including a description of the sampling sites with numerous figures and tables, are provided in *SI Appendix*. Two unique methods were used. The e/i-DNA methodology is described in detail in an appropriate subject journal (13), with some of the associated issues discussed elsewhere (40). The validity of the e/i-DNA method is further supported by a

positive correlation between microbial biomass and the Shannon index (SI) calculated for iDNA ($r = 0.62$), but not with either calcium or sulfate concentrations. Conversely, the SI for eDNA correlated with calcium and sulfate soil concentrations ($r = 0.74$ and 0.61, respectively), but not with biomass ($r = 0.03$). The other state-of-the-art method was used to measure in situ replication rates of genomes by calculating the number of active replication forks reconstructed from the metagenome sequences (15) (see *SI Appendix, Read-Based Metagenomics, Genome-Resolved Metagenomics and in Situ Replication Rates* for more details). All data reported in this paper are compiled in *SI Appendix* and have been archived at GenBank/EMBL under BioProject ID PRJNA395196 and at EMBL-EBI under accession no. PRJEB20402 (sample IDs ERS1666624–ERS1666714).

ACKNOWLEDGMENTS. D.S.-M. acknowledges support by the European Research Council Advanced Grant Habitability Of Martian Environments (339231), which provided base funding for the study, including sample collection. The fungal diversity assessment was supported by funding (to H.-P.G.) through the Leibniz Senatsausschuss Wettbewerb Project MycoLink and DFG Project Microprime (GR1540/23-1). F.K. received financial support from the German Science Foundation (DFG KE 884/8-2). The 16S rRNA gene amplicon (MiSeq) sequencing was financed through the Helmholtz Research Program "Geosystem–The Changing Earth" and the data were processed by Fabian Horn (GFZ German Research Center for Geosciences–Helmholtz Center Potsdam). The stable isotopic composition of water was carried out through the Europlanet 2020 Research Infrastructure supported by the European Union's Horizon 2020 research and innovation program (654208). Endospore quantification benefited from funding by the Deep Carbon Observatory through a Pilot Project (L.W.). Part of the organic geochemical analyses were performed at Imperial College London, supported by United Kingdom Space Agency Grant ST/N000560/1. V.P. and D.C.'s work was supported by the Spanish Ministry of Economy and Competitiveness Grants ESP2015-69540-R and RYC-2014-19446, respectively. G.V. was supported by a Humboldt Research Fellowship for postdoctoral researchers. M.F. acknowledges support from National Institute of Food and Agriculture Hatch Project 1014527. The Leibniz Institute of Freshwater Ecology & Inland Fisheries (IGB) housed the workshop at which much of the presented work was coordinated. We thank M. Degebrodt for technical assistance.

1. Ewing SA, et al. (2006) A threshold in soil formation at Earth's arid-hyperarid transition. *Geochim Cosmochim Acta* 70:5293–5322.
2. Michalski G, Boehlke JK, Thiemens M (2004) Long term atmospheric deposition as the source of nitrate and other salts in the Atacama Desert, Chile: New evidence from mass-independent oxygen isotopic compositions. *Geochim Cosmochim Acta* 68:4023–4038.
3. Davila AF, Schulze-Makuch D (2016) The last possible outposts for life on Mars. *Astrobiology* 16:159–168.
4. Wierzchos J, et al. (2011) Microbial colonization of Ca-sulfate crusts in the hyperarid core of the Atacama Desert: Implications for the search for life on Mars. *Geobiology* 9:44–60.
5. Crits-Christoph A, et al. (2013) Colonization patterns of soil microbial communities in the Atacama Desert. *Microbiome* 1:28.
6. Azua-Bustos A, Caro-Lara L, Vicuna R (2015) Discovery and microbial content of the driest site of the hyperarid Atacama Desert, Chile. *Environ Microbiol Rep* 7:388–394.
7. Navarro-Gonzalez R, et al. (2003) Mars-like soils in the Atacama Desert, Chile, and the dry limit of microbial life. *Science* 302:1018–1021.
8. Stevenson A, et al. (2015) Multiplication of microbes below 0.690 water activity: Implications for terrestrial and extraterrestrial life. *Environ Microbiol* 17:257–277.
9. Bozkurt D, Rondanelli R, Garreaud R, Arriagada A (2016) Impact of warmer eastern tropical Pacific SST on the March 2015 Atacama floods. *Mon Weather Rev* 144:4441–4460.
10. Normand P (2006) *Geodermatophilaceae* fam. nov., a formal description. *Int J Syst Evol Microbiol* 56:2277–2278.
11. Montero-Calasanz MdC, et al. (2013) *Geodermatophilus tzadiensis* sp. nov., a UV radiation-resistant bacterium isolated from sand of the Saharan desert. *Syst Appl Microbiol* 36:177–182.
12. Ewing SA, et al. (2007) Rainfall limit of the N cycle on Earth. *Glob Biogeochem Cycles* 21:GB3009.
13. Alawi M, Schneider B, Kallmeyer J (2014) A procedure for separate recovery of extra- and intracellular DNA from a single marine sediment sample. *J Microbiol Methods* 104:36–42.
14. Levy-Booth DJ, et al. (2007) Cycling of extracellular DNA in the soil environment. *Soil Biol Biochem* 39:2977–2991.
15. Robinson CK, et al. (2015) Microbial diversity and the presence of algae in halite endolithic communities are correlated to atmospheric moisture in the hyper-arid zone of the Atacama Desert. *Environ Microbiol* 17:299–315.
16. Finstad KM, et al. (2017) Microbial community structure and the persistence of cyanobacterial populations in salt crusts of the hyperarid Atacama desert from genome-resolved Metagenomics. *Front Microbiol* 8:1435.
17. Kuske C, et al. (1998) Small-scale DNA sample preparation method for field PCR detection of microbial cells and spores in soil. *Appl Environ Microbiol* 64:2463–2472.
18. Hertkorn N, et al. (2008) Natural organic matter and the event horizon of mass spectrometry. *Anal Chem* 80:8908–8919.
19. Rossello-Mora R, et al. (2008) Metabolic evidence for biogeographic isolation of the extremophilic bacterium Salinibacter ruber. *ISME J* 2:242–253.
20. Maslov S, Sneppen K (2017) Population cycles and species diversity in dynamic Kill-the-Winner model of microbial ecosystems. *Sci Rep* 7:39642.
21. Thingstad TF (2000) Elements of a theory for the mechanisms controlling abundance, diversity, and biogeochemical role of lytic bacterial viruses in aquatic systems. *Limnol Oceanogr* 45:1320–1328.
22. Fierer N, et al. (2007) Metagenomic and small-subunit rRNA analyses reveal the genetic diversity of bacteria, archaea, fungi, and viruses in soil. *Appl Environ Microbiol* 73:7059–7066.
23. Tyson GW, et al. (2004) Community structure and metabolism through reconstruction of microbial genomes from the environment. *Nature* 428:37–43.
24. Brown CT, Olm MR, Thomas BC, Banfield JF (2016) Measurement of bacterial replication rates in microbial communities. *Nat Biotechnol* 34:1256–1263.
25. Wilson SA, Bish DL (2011) Formation of gypsum and bassanite by cation exchange reactions in the absence of free-liquid H_2O: Implications for Mars. *J Geophys Res* 116:E09010.
26. Palacio S, Azorín J, Montserrat-Martí G, Ferrio JP (2014) The crystallization water of gypsum rocks is a relevant water source for plants. *Nat Commun* 5:4660.
27. Davis WL, de Pater I, McKay CP (2010) Rain infiltration and crust formation in the extreme arid zone of the Atacama Desert, Chile. *Planet Space Sci* 58:616–622.
28. Warren-Rhodes KA, et al. (2007) Cyanobacterial ecology across environmental gradients and spatial scales in China's hot and cold deserts. *FEMS Microbiol Ecol* 61:470–482.
29. Bates ST, et al. (2011) Examining the global distribution of dominant archaeal populations in soil. *ISME J* 5:908–917.
30. Smith DJ, Griffin DW, Schuerger AC (2010) Stratospheric microbiology at 20 km over the Pacific Ocean. *Aerobiologia* 26:35–46.
31. Rajeev L, et al. (2013) Dynamic cyanobacterial response to hydration and dehydration in a desert biological soil crust. *ISME J* 7:2178–2191.
32. Hua X, Huang L, Tian B, Hua Y (2008) Involvement of recQ in the ultraviolet damage repair pathway in Deinococcus radiodurans. *Mutat Res* 641:48–53.
33. Ming DW, et al. (2014) Volatile and organic compositions of sedimentary rocks in Yellowknife Bay, Gale crater, Mars. *Science* 343:1245267.
34. Neilson JW, et al. (2017) Arid soil microbiome: Significant impacts of increasing aridity. *mSystems* 2:e00195.
35. Craddock RA, Lorenz RD (2017) The changing nature of rainfall during the early history of Mars. *Icarus* 293:172–179.
36. Spiga A, et al. (2017) Snow precipitation on Mars driven by cloud-induced night-time convection. *Nat Geosci* 10:652–657.
37. Möhlmann DT, Niemand M, Formisano V, Savijrvi H, Wolkenberg P (2009) Fog phenomena on Mars. *Planet Space Sci* 57:1987–1992.
38. Malin MC, Edgett KS (2000) Evidence for recent groundwater seepage and surface runoff on Mars. *Science* 288:2330–2335.
39. Bish DL, Carey JW, Vaniman DT, Chipera SJ (2003) Stability of hydrous minerals on the Martian surface. *Icarus* 164:96–103.
40. Vuillemin A, et al. (2017) Preservation and significance of extracellular DNA in ferruginous sediments from Lake Towuti, Indonesia. *Front Microbiol* 8:1440.

PNAS Supporting Information: A Transitory Microbial Habitat in the Hyperarid Atacama Desert

Schulze-Makuch et al. 10.1073/pnas.1714341115

Material and Methods

Site Descriptions (WGS84 = World Geodetic System 1984, m a.s.l. = meters above sea level). All study site locations are depicted in Fig. S1.

Coastal Soil (CS): 481 m a.s.l., S 23.8247, W 70.4888 (WGS84) The Coastal Soil site (see image below) is located 21 km south of Antofagasta and 1 km inland from the shoreline and about 50 m behind the first ridge of the coastal range. This location is subject to frequent coastal fog and occasional rain events, indicated by widely spaced vegetation growth and distinct hypolithic microbial communities. The sampled pit is located on the very proximal part of an alluvial fan with a local slope of 11^o. The surface is covered by very angular lithic clasts of up to 50 cm in diameter originating approximately 100 m upslope from bedrock outcrops. The top 20 cm are composed of silty-to-sandy material containing occasional few-cm large weathered clasts of reddish surface color. The top 40 cm are dispersed with very fine, hair-like roots. Below 40 cm depth the soil becomes moist and the fraction of very angular clasts increases rapidly. From a depth of about 60 cm, the soil transitions into fractured bedrock with little soil infill and greyish color.

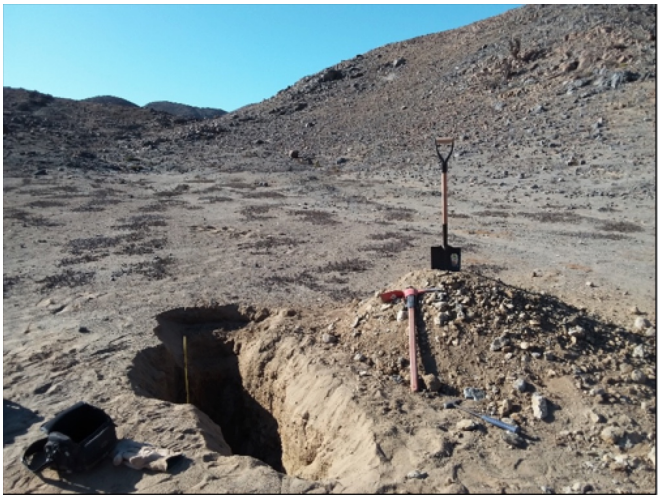

Alluvial Fan (AL): 847 m a.s.l., S 24.0008, W 70.2958 (WGS84) The Alluvial Fan site (see image below) is located on the eastern slope of the coastal range, 22 km inland from the shoreline and protected from direct ocean moisture (e.g. spray). Nevertheless, moisture supply derives from occasional fog events following a ∼38 km long morphology-driven fog path. In the uppermost part of the alluvial fan the surface is populated by shrubs as well as by less distinct hypolithic cyanobacteria thriving on the bottom side of a few dispersed surficial quartz clasts, indicating at least some occasional presence of water. The sample pit lies in the mid-section of the alluvial fan, with a local slope of 8.5^o, between two shallow alluvial gullies approximately 20 m apart. The surface is covered with loose sandy sediment with dispersed subangular clasts reaching up to 15 cm in diameter. Below the top layer of loose soil lies a few cm thick vesicular evaporitic layer. Below these upper units, down to 100 cm, the soil consists of alluvial deposits which vary horizontally, distinguishable by their maximum grain size. The individual horizons are crudely layered and vary in maximum grain size from coarse sand to cobbles embedded in a fine, unconsolidated and uncemented matrix consisting of clay and silt. Laterally discontinuous halite cemented lenses (30 cm in diameter and 10 cm thick) occur at a 40 cm depth.

Red Sands (RS): 1027 m a.s.l., S 24.1007, W 70.1288 (WGS84) The Red Sands site (see image below) is located 38 km inland from the shoreline, in the western Yungay Valley, on the distal part of a south-facing Holocene alluvial fan incised by shallow channels. Vegetation and hypoliths are not visible, indicating a lower water supply than at the Alluvial Fan site (due to the ∼60 km long fog path). The pit is located between the most recent generations of channels. The top layer consists of a cemented desert crust, a few cm thick with embedded pebble and cobble clasts. Down to 30 cm depth the sediment is composed of poorly sorted sand with crude lamination. At a depth of 40 cm the sediment is more intensely cemented. Clasts and sand particles are coated with a thin evaporitic crust or a desert varnish. Below this layer, at a depth of 50 cm, the sediment becomes less cemented and increases in clast size. At a depth of 90 cm lies a highly competent halite-cemented sediment horizon extending to a

depth of at least 100 cm.

Maria Elena (ME): 1313 m a.s.l., S 22.2631, W 69.7243 (WGS84) The Maria Elena site (see image below) is located 50 km inland from the shoreline in the hyperarid core of the Atacama Desert on an alluvium with a slope of 6.7^o. The surface is covered with cobbles and boulders reaching a few meters in diameter. They originate from outcrops located on hills about 2 km to the north and occur exclusively on top of the soil, suggesting that earthquake-driven kinetic sieving prevents them from being buried. Most of the boulders are less than 1 m apart and frequently touch where earthquake-driven rubbing faces are visible.

The top soil between the boulders is covered with a single layer of loose detrital ranging from coarse sand to fine pebbles being too large for aeolian transport. The uppermost 20 cm of the pit are reddish to light brown in color and consist of weakly cemented silt to coarse sand showing abundant planar and cross-bedding. The sediment below does not change in particle size and composition and shows no laminations. Furthermore, the color transitions sharply into a whitish light brown due to a moderate cementation, which fades away with depth. Below a depth of 70 cm the soil is intensely cemented, transitioning from brittle material to a hardground that fractures into large blocks. Rarely occurring vertical sand-filled fractures originate at the top with a width of a few cm and pinch out at a depth of about 50 cm.

Yungay (YU): 1004 m a.s.l., S 24.0883, W 69.9946 (WGS84) The Yungay site (see image below) is located on the distal part of an alluvial fan 50 km inland from the coastline with a local slope of 1.27^o. The fog path coming directly from the west is ∼73 km long, but since the Yungay site is located behind a topographic high in the Yungay valley, fog may also reach the Yungay site from the east via a ∼100 km long fog path. However, vegetation and hypoliths are not visible.

The surface near the pit is covered with isolated, lithological divers, partially venti-faced clasts ranging in size from cobbles to boulders. They rest on top of a ∼10 cm thick unconsolidated layer of mostly lithic particles ranging in size from silt to pebbles, called *chuca*. Embedded in the *chuca* layer are evenly spaced, 5 to 20 cm wide and a few cm thick, partially cracked, patty-shaped sulfate mineral bearing lobes, called *losa*.

Below this loose layer lies a few cm-thick brittle, highly porous, vesicular gypsum horizon, followed by a polygonal cracked sulfate hardpan. The ∼1 m diameter polygons are dominated at the top by gypsum-containing, isolated, highly angular and poorly sorted sand-to-cobbles. At a depth of 40 to 60 cm the gypsum transitions into anhydrite, while the fraction of coarse lithic sand increases, becoming the main constituent below a depth of 80 cm. The sulfate polygons are separated by sand dikes up to 20 cm wide and 80 cm deep that taper off with depth and show a crude vertical stratification.

Lomas Bayas (LB): 1528 m a.s.l., S 23.3933, W 69.6039 (WGS84) The Lomas Bayas site (see image below) is located at the hyperarid core of the Atacama Desert ∼80 km inland from the shoreline on the proximal part of an alluvial fan with a slope of 3.7^o. The surface is largely covered by very angular clasts of up to 40 cm in diameter originating approximately 400 m upslope from bedrock outcrops. The pebble- to cobble-sized clasts are coated with dark desert varnish and frequently have ventifact morphology. At the location of the pit the surficial clasts are widely spaced and the surface is largely covered by sandy to gravely material. In the near surrounding of the pit (5-10 m) pebble- to cobble-sized clasts have developed a densely packed rock pavement. Down to a depth of 1 m the soil is composed of clay- to cobble-sized particles of angular shape and poor to no sorting, analogous to the modern composition of the top surface. Except for crude lamination in the top few cm the entire 1 m deep soil profile

shows no sedimentary bedding. Down to a depth of about 40 cm the soil is very loose, followed by minor cementation and hardening of the ground.

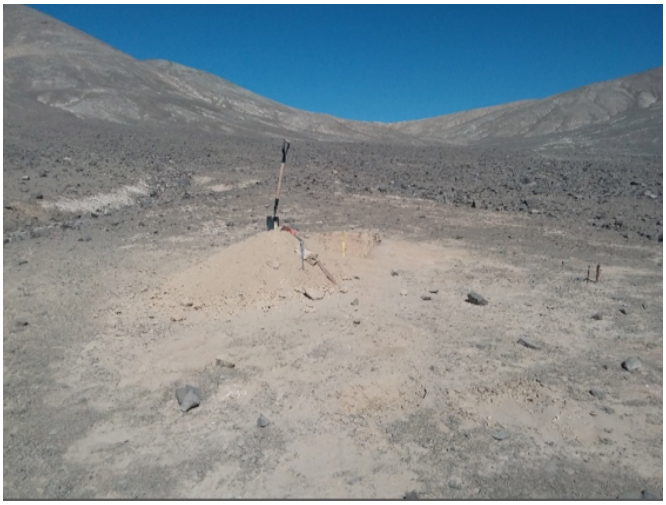

Climate and UV Field Measurements. Biologically relevant niches were identified and habitats are characterised by their macro- and microclimate. Various parameters directly affecting the microclimate, the survival capacity and vitality of the microorganisms (e.g. cyanobacteria, lichens, bacteria and archaea) colonizing Atacama habitats were measured. Diurnal bio-relevant UV B radiation dose and fluency, together with the relative humidity and temperature at the sample sites, were measured with a PMA 2100 (Fa. SOLAR Light / Optopolymer, Munich, Germany). The data was collected electronically and analysed. Photosynthetically active radiation (PAR) and the temperature of the rocks and air in the microenvironment was measured with a Mini-PAM device (Heinz Walz GmbH, Erlangen, Germany).

Soil parameters.

Water Content. Water content of soil samples was determined gravimetrically. Soil samples were oven-dried susequently at 60^{o}C and 105^{o}C, each for 24 hrs. After drying, samples were cooled in a desiccator. The gravimetric water content was determined based on the weight differences between initial and dried samples. The 60^{o}C drying was used to differentiate between structural water in gypsum in comparison to bassanite, which formed after drying at 105^{o}C.

Moisture Sorption Isotherms and Water Activity. Moisture sorption isotherms were determined with an AquaSorb Isotherm Generator (Decagon Devices, Inc., Pullman, WA). Water activity was measured with a chilled-mirror dew point sensor, and water content with a high precision magnetic force balance. Water activity measurements were verified with KCl, NaCl and LiCl standard solutions. About 1.5 g of soil were first oven-dried at 105^{o}C for 24 hrs and then cooled in a desiccator for a few minutes. Soil samples were then inserted into the AquaLab instrument and an adsorption isotherm was determined, followed by a desorption isotherm. The maximum water activity was set to a_w = 0.88 to 0.89. Higher water activities could not be determined due to instrumental limitations for water activities above 0.88. Air flow was set to 250 mL/min and operating temperature was 25^{o}C. Water activity of the soil samples taken from the field was determined from the measured water contents at 105^{o}C and the moisture sorption isotherms. Because the moisture sorption isotherms are hysteretic, there are two water activities (one for adsorption, and one for desorption), associated with each water content measurement. Fig. S2 shows the plot of water content at both 60^{o}C and 105^{o}C on April 21-28, 2015 along with corresponding water activity of the desorption isotherm.

Geochemical and Mineralogical Analysis. To provide a geochemical and mineralogical context for the collected soil samples, we performed analyses by ion chromatography (IC) to determine the main soluble inorganic and organic ions, and X-ray diffraction (XRD) to determine the dominant mineral phases.

Inorganic Salts. For each sample, 1.0 g was leached with water (Nanopure 18.2 MΩ-cm) for 1 hour with gentle stirring. The leachate was then removed and filtered using a 0.2 μm PTFE filter. Samples prepared for perchlorate analysis were leached at a 1:5 (wt/vol) ratio and samples for inorganic anion and cation analysis were leached at a 1:10 (wt/vol) ratio and diluted to a conductivity of ∼50 μS/cm. Soluble inorganic content was determined by ion chromatography (IC) using a Dionex ICS-2000 Reagent Free IC equipped with suppressed electrical conductivity detection. Separation and detection of perchlorate, inorganic anions, and inorganic cations was achieved as follows: for perchlorate we used a 100 μL injection volume and a Dionex AS18 Ionpac analytical column with 35 mM potassium hydroxide (KOH) eluent at a flow rate of 1.25 mL/min and a suppressor current of 100 μS; for cations we used a 25 μL injection volume, an AS16 column with 20 mM KOH at a flow rate of 1.0 mL/min and suppressor current of 75 μS for anions; and a 25 μL injection volume, a CS12 column with 23 mM methyl sulfonic acid at 1.0 mL/min and a suppressor current of 59 μS.

Organic Salts. Two grams of sample were dissolved in 40 mL of distilled water under agitation for 24 hours in a 50 mL capacity conical tube. The tubes were centrifuged at 4000 g for 10 min to remove mineral particles. The supernatants were collected (10 mL) and set undiluted and at two different dilutions (1/2 vol/vol and 1/5 vol/vol) into a sample holder for automatic loading into a Metrohm 861 Advanced Compact Ion Chromatographer IC (Metrohm AG, Herisau, Switzerland). Anions were determined using a *Metrosep A supp* 7-250 column with 3.6 mM sodium carbonate ($NaCO_3$) as eluent. Calibration curves were performed for a set of compounds separately and in mixtures: fluoride, chloride, bromide, nitrite, nitrate, phosphate, sulfate, acetate, formate, propionate, tartrate, and oxalate. Only values that fit in the linear part of the calibration curves were considered.

Mineralogy. To obtain a fine powder, 5-10 g of sample were ground in a disk mill for 20 seconds at 750 rpm prior to passing it through a 63 μm mesh. The powder was then loaded onto the holder for X-Ray Diffraction (XRD). XRD was performed using a Seifert 3003 TT with Cu Kα radiation (λ = 1.542 Å). The X-ray generator was set to an acceleration voltage of 40 kV and a filament emission of 40 mA. Samples were scanned between 5^o (2θ) and 60^o (2θ) using a step size of 0.1^o (2θ) and a count time of 2 s. For determining the salt mineralogy

bulk samples were desiccated and ground soundly with an agate mortar and subsequently analyzed with a PANalytic Empyrean powder X-ray diffractometer (XRD). The x-ray source is a Cu-Kα radiation performing 40 kV and 40 mA scanning 10^o to 100^o 2θ in a step interval of 0.013^o 2θ with a step-counting time of 20 s. The XRD data was evaluated semi quantitatively with the WinPLOTR (FullProf) software calculating the intensity of the specific gypsum (11.59^o 2θ) and anhydrite (25.50^o 2θ) XRD peaks by using a pseudo-Voigt function in order to determine the ratio of peak intensity.

Inorganic Isotope Geochemistry. Water isotope analysis was performed following the standard extraction procedure described previously (1). Briefly, 20 to 50 g of samples kept in sealed plastic containers were loaded in glass or steel vessels under dry atmosphere and then pumped to reach pressure $<10^{-2}$ mbar. Under static vacuum, water was thermally extracted (110^oC) and transferred cryogenically. After 3 days water was weighed and transferred for isotopic analysis. D/H & $^{18}O/^{16}O$ ratios were measured by CRDS, using a Picarro L2140-I installed at CRPG, and expressed in delta notation on the V-SMOW - VSLAP scale. Long term reproducibility is better than 1 and 0.1‰ for δD and δ^{18}O, respectively at 95 % confidence level. Fe isotopes of bulk sample were measured and quality checked by processing IFG standard that returned δ^{56}Fe & δ^{57}Fe within 0.02‰ of literature values (2). Sulfate from samples (from 2-10 g) was dissolved in ultra-pure water (ion chromatography quality), acidified with HCl (1 M), and boiled until an acidic pH was achieved, followed by precipitation of $BaSO_4$, which was used for sulfur and oxygen analysis. The sulfur isotopes ($^{34}S/^{32}S$ ratio expressed as δ^{34}S on the CDT scale) and oxygen isotopes ($^{18}O/^{16}O$ ratio expressed as δ^{18}O on the VSMOW scale) were analyzed using IRMS (MAT 253 at INTA-CSIC).

Organic Analyses.

TOC Methodology. To determine the amount of total organic carbon (TOC), 15 to 30 mg of each soils sample were sieved to remove grains larger than 2 mm in diameter. Subsequently, samples were milled to a powder and dried at 105^oC for 3 to 5 hours. TOC was measured with a "Vario EL III Elemental Analyzer" from "Elementar Analysesysteme GmbH" by heating the sample to 550^oC under an oxygen atmosphere. Evolving CO_2 amount was determined with an thermoconductivity detector cell.

Solvents and Reagents. All solvents used, dichloromethane (CH_2Cl_2), methanol (CH_3OH) and toluene were purchased from Fisher Scientific and were of spectroscopic grade. Water was purified using a Neptune Purite pure water purification system.

Extraction Protocol. Approximately 5.0 g masses of all of the soil samples were weighed and placed in 50 mL stoppered flasks, then 20 mL of solvent(s) was added and the mixture was shaken (400 rpm) at RT for 72 hours. The solvents system used was toulene/CH_3OH 2:1 v/v, for the extraction of particularly lipophilic organic compounds. The samples were then filtered, and the filtrates evaporated in vacuo. For GC-MS analysis, the residues were dissolved in 5mL CH_2Cl_2. All prepared GC-MS samples were stored at -18^oC prior to use.

Instrumentation. An Agilent 6890 GC setup was used. The Atacama Desert soil extracts, dissolved in DCM (1.0 mL vial sample) were introduced to the GC via split injection with a 50:1 split ratio with the injector at 270^oC and the inlet temperature of 350^oC. Separation was performed on a J&W DB-5MS Ultra Inert column (30 m $\times$ 0.25 mm i.d $\times$ 0.25 μm). Helium at column flow rate of 2 mL/min (constant flow rate) was used as the carrier gas. The GC oven temperature was held for 2 min at 50^oC and then raised at 4^oC/min to 310^oC, and the final temperature was held for 20 minutes. The GC was coupled to an Agilent 5973 inert mass spectrometer. The MS was run in full scan mode (10-200 amu) at 3.7 Hz. All compounds were identified from the obtained mass spectra by reference to the NIST library and all have a NIST similarity score of $>$ 90 %.

Emission Rates of Chloromethane GC-MS. Samples of the headspace from the pyrolysis reactor were removed and transferred to a cryogenic pre-concentration unit (3) which was connected to a gas chromatograph mass spectrometer (Varian Star 3400 GX gaschromatograph, Varian Saturn 2000 ion trap massspectrometer). The gas chromatograph was fitted with a BP624 column (30 m; 0.32 mm i.d.; 1.8 μm; SGE Analytical Science) followed by a DB5 (60 m; 0.32 mm i.d.; 1 μm; SGE Analytical Science). The temperature was isothermally held at 30^oC for 22.5 min and afterwards heated with 30^oC min^{-1} to 210^oC as final temperature, which was held for 10 min. For identification of analytes, the mass spectrometer was operated measuring ion currents between 47 and 249 atomic mass units (amu). CH_3Cl was identified both by its retention time and mass spectrum and quantification was performed using ion currents at m/z 50 and 52 amu. To quantify the peak area for ion m/z 50 and 52 amu at the expected retention time of CH_3Cl was compared to a standard response curve. Its detection limit was 0.3 ng. Control samples were prepared and treated in an identical fashion to that of the samples except that no soil was added to the pyrolysis tube.

Extraction and Analysis of Polycyclic Aromatic Hydrocarbons (PAHs). Soil samples (between 20 and 45 g) were extracted by Accelerated Solvent Extraction (ASE 300 Dionex) twice with acetone at 100^oC each time for 10 min followed by a second extraction step with toluene at 150^oC, also twice for 10 min. Extracts were concentrated to 1 mL under nitrogen. A gas chromatograph (GC 6890 Hewlett Packard) equipped with a split-splitless injector and mass-selective detector (MSD 5973 Hewlett Packard) was used for quantification. Sample injection volume was 1 μL. A DB-5MS fused-silica capillary column (Agilent J&W GC Columns, 30 m length, 0.25 mm ID and 0.25 μm film thickness) served for separation of the compounds. The injector was maintained at 250^oC and the transfer line at 315^oC. Oven temperature was initially held at 65^oC for 4 min, then increased at a rate of 10^oC/min to 270^oC held for 10 min, and finally to 310^oC held for a further 6.5 min. Helium was used as carrier gas with a constant flow of 1 mL/min. The detector was operated in Selected Ion Mode (SIM). For quantification, internal standards of per-deuterated PAHs (Acenaphthene D10, Chrysene D12, Naphthalene D8, Perylene D12, Phenanthrene D10) were used.

Stable Hydrogen Isotope Measurements of Chloromethane (GC-IRMS). A cryogenic pre-concentration unit with several purification and concentration stages was designed

and built in-house. A detailed description of the system is provided in Greule et al. (4). The cryogenic pre-concentration unit was coupled directly to a Hewlett Packard HP6890 gas chromatograph (Agilent Technologies, Palo Alto, USA) which was interfaced with an Isoprime IRMS via a 1050^{o}C GCV high-temperature conversion reactor (Isoprime, Manchester, UK). The GC was equipped with a GasPro column (60 m $\times$ 0.32 mm i.d.; Agilent Technologies, Palo Alto, USA) and was held isothermally at either 70 or 150^{o}C. The pyrolysis reactor contained a 0.65 mm i.d. quartz tube packed with chromium pellets (Isoprime, Manchester, UK). The helium flow from the pre-concentration unit was set to 1.0 mL min^{-1}. A tank of ultrahigh-purity hydrogen (Hydrogen 5.0, Air Liquide, Düsseldorf, Germany) with a certified δ^2H V-SMOW value of -172 $\pm$ 2 ‰ (certificated by Air Liquide) was used as the working reference gas. The $H3^+$ factor, determined daily during this investigation (3 month period), was in the range 4.79-5.00 ppm/nA. The conventional 'delta' notation, which expresses the isotopic composition of a material relative to that of a standard on a per mil (‰) deviation basis, was used. The stable hydrogen isotope value for the local CH_3Cl reference was -117.1 ‰. The method allows determination of isotopic values of samples ranging from -100 to -300 ‰ with typical standard deviations better than $\pm$3 ‰ for δ ^{2}H CH_3Cl values. Hydrogen isotope signatures of the bulk methoxyl pool, including esterified and ether bonded methyl groups (also methyl thioesters), of the soil samples were measured as CH_3I released upon treatment of the samples with HI. The procedure employed was that of Greule et al. (4) except that larger samples of headspace were withdrawn and pre-concentrated using the above described cryogenic pre-concentration unit. Hydriodic acid (HI, 0.5 mL, 55-58 %) was added to the sample (5 to 1000 mg) in a glass vial (5 mL). The vials were sealed with caps containing PTFE lined butyl rubber septa and incubated for 30 min at 130^{o}C. After heating, the vials were allowed to equilibrate at room temperature (22$\pm$0.5^{o}C, air conditioned room) for at least 30 min before a sample of headspace was transferred to cryogenic pre-concentration unit and the GC-TC-IRMS system. The primary reference working standard for reporting on the VSMOW scale was CH_3I with a measured value of -179.0 $\pm$ 2.9 ‰. The δ ^{2}H value of this standard (δ^2H_{CH3I}) was calibrated against international reference substances (IAEA-CH-7 [δ^2H_{VSMOW}: -100.3 ‰], NBS-22 [δ^2H_{VSMOW}: -118.5 ‰]) and a tertiary standard (IA-R002, purchased from Iso-Analytical Ltd, Sandbach, UK [δ^2H_{VSMOW}: $-$111.2 ‰]) using an EA-IRMS system configured for δ^2H measurements (elemental analyser-isotopic ratio mass spectrometer, Iso-Analytical Ltd, Sandbach, UK).

DNA isolation and sequencing.

Extraction of extracellular (e) and intracellular (i) DNA. To facilitate DNA extraction from the sediment samples, with very low DNA concentrations, the protocol from Alawai et al. (5) was slightly modified as described below. All DNA extractions were performed in triplicates and included blank controls for iDNA and eDNA.

Cell separation. In a 15 mL sterile conical tube 6.5 g of Atacama Desert soil sample and 0.4 g Polyvinylpolypyrrolidone (PVPP, Sigma-Aldrich order No. 77627 (6)) were carefully suspended in 5-6 mL of cold (4^{o}C) sodium phosphate (NaP) buffer (Na_2HPO_4 and NaH_2PO_4, 0.12 M, pH 8), to form a slightly viscous slurry (7). The tube was chilled on ice for 1 min and then shaken twice for 5 min at 150 rpm in a horizontal position on an orbital shaker with cooling on ice in between for 3 min. After a centrifugation step (500 g, 4^{o}C, 10 min, swing-out rotor) the supernatant was transferred to a sterile 15 mL conical tube and kept on ice. The remaining pellet was resuspended in 3.0-3.5 mL NaP buffer and the separation procedure was repeated three more times with all supernatants pooled in one tube (6-8 mL). After centrifugation (4,643 g, 4^{o}C, 1 h, swing-out rotor) the supernatant representing the eDNA fraction was transferred to a new tube and the pellet containing the intact cells with the iDNA were kept on ice. The supernatant was passed through a 0.2 μm syringe filter (VWR international, cellulose acetate) pre-rinsed with 500 μL NaP buffer. After passing the sample, the filter was rinsed with another 500 μL NaP buffer and then added to the filtered eDNA solution. The filtrate was collected in a sterile 50 mL conical tube and kept on ice until further processing.

The iDNA containing pellet was carefully resuspended in 1 mL NaP buffer, transferred to a sterile 2 mL reaction vial (Eppendorf, low binding) and centrifuged for 20 min at 12,000 g to remove any remaining eDNA. The supernatant was discarded and the pellet suspended in 750 μL NaP buffer by incubation in a thermal shaker for two periods of 5 min at 70^{o}C and 250 rpm with cooling on ice in between for 2 min. The suspension was transferred to a PowerBead tube (Mo Bio laboratories, Inc.) (buffer removed), mixed with 60 μL solution C1 (PowerSoil Kit, Mo Bio) and vortexed horizontally for 10 min according to the kit instructions. After centrifugation (10,000 g, 1 min) the supernatant was transferred to a new low binding 2 mL reaction vial and mixed with 250 μL solution C2 (vortex 5 s; incubation 5 min, 4^{o}C; centrifugation at 10,000 g, 1 min). The supernatant (ca.1 mL) was kept on ice in a 50 mL sterile conical tube.

Recovery of iDNA and eDNA. iDNA and eDNA solutions were each mixed with the threefold amount of Guanidine hydrochloride (GuaHCl) (6M GuaHCl in TE buffer, pH 6.7, 10 mM Tris HCl, 1 mM EDTA) and 15 μL (iDNA) or 18 μL (eDNA) silica suspension (preparation according to Alawi et al. (5)) by inverting the tubes several times. The tubes were secured horizontally on an orbital shaker and shaken for 45 min and 175 rpm to bind the DNA to the silica particles. Finally the silica was allowed to settle for 10 min on ice before the centrifugation step (4,643 g, 10 min, RT, swing-out rotor). The supernatants were carefully removed by suction except for a residual of 1.5 mL to resuspend the silica pellets. The suspensions were transferred to new sterile 2 mL low binding reaction vials and centrifuged (9,000 g, RT, 3 min). The supernatants were discarded and the pellets were each washed with 600 μL washing buffer (55 % EtOH, 70 mM NaCl, 10 mM Tris, 2.6 mM EDTA) (vortex 2 s, centrifuge at 9,000 g, 1 min). The resulting supernatants were discarded, the pellets were again centrifuged (9,000 g, RT, 3 min) and the remaining buffer was removed. The pellets were air-dried in a clean bench for 15 min. Finally the DNA was eluted by resuspending the pellets in 100 μL (eDNA) or 80 μL (iDNA) Tris buffer (1 mM Tris, pH 8.0, preheated to 50^{o}C) by pipetting up and down, vortex 2 s, followed by an incubation period of 10 min in a thermal shaker (50^{o}C, 300 rpm). The silica suspensions

were centrifuged (9,000 g, RT, 2 min) and the supernatants were transferred to new 1.5 mL low binding reaction vials. To remove any residual silica particles the supernatants were centrifuged again (9,000 g, RT, 5 min) and were transferred to new vials. DNA concentrations were mostly below the detection limit of fluorometric quantification methods.

Quantitative PCR analysis (qPCR). qPCR was performed using a CFX Connect Real-Time PCR Detection System (Bio-Rad, CA, USA) in duplicates of iDNA and eDNA and corresponding blank controls using iTaq Universal SYBR Green Supermix (Bio-Rad). DNA was amplified with the universal primers 331F and 797R (8) and the following cycling parameters: initial denaturation at 95^{o}C, 4 min followed by 40 cycles (95^{o}C, 30 s; 58^{o}C, 30 s; 72^{o}C, 30 s; 80^{o}C, 3 s). The correlation coefficient for the standard curves was $\geq$0.99 and the PCR efficiency was on average 90 %. The standard was a known concentration of a 16S rRNA gene PCR fragment of *Bacillus subtilis*.

16S rRNA gene amplicon pool preparation for Illumina MiSeq sequencing. PCR amplification targeted the hypervariable region V4 of the 16S rDNA (forward primer, 515F: 5'-GTGCCAGCMGCCGCGGTAA-3'; reverse primer, 806R: 5'-GGACTACHVGGGTWTCTAAT-3', each of them specified with 6-bp tags). PCR amplification was performed in at least triplicate in 25 μL reactions (2.5 μL 10x PCR buffer, 0.5 μL ultrapure dNTP-mix (5 mM), 0.25 μL of each primer (10 mM), 1.5 μL $MgCl_2$ (25 mM), 2-5 μL template, 0.25 μL HotStar *Taq* polymerase (Qiagen, Hilden, Germany)) under the following conditions: initial denaturation at 95^{o}C for 15 min, followed by 10 cycles of 95^{o}C for 30 s, 65^{o}C -1^oC/cycle for 30 s, 72^{o}C for 45 s, 25 to 40 cycles (depending on DNA concentration of the different samples) of 95^{o}C for 30 s, 56^{o}C for 30 s, 72^{o}C for 45 s, and a final extension step of 10 min at 72^{o}C . The reactions were pooled, purified with Agencourt AMPure XP magnetic beads (Beckman Coulter, CA, USA), and quantified with the Qubit Fluorometer (Invitrogen, Thermo Fisher Scientific, USA). Purified PCR amplicons from all samples were pooled in equimolar ratios to a final concentration of approximately 120 ng/μL. Library preparation and sequencing of the amplicon pool with the Illumina MiSeq technology was done by Eurofins Genomics (Ebersberg, Germany).

Processing of 16S rDNA MiSeq data. Quality of the raw data was checked using *fastqc* tool for high throughput sequence data (www.bioinformatics.babraham.ac.uk/projects/fastqc/). Sequences were demultiplexed and the barcodes were removed with the *CutAdapt* tool [trim-n; e 0.1; only consider exact barcodes for mapping (9)]. Reads were assembled by overlapping sequence regions using PEAR [Q25; p 0.0001; v 20 (10)]. Standardization of the nucleotide sequence orientation were done using an in house script. Trimming and filtering of low quality sequences were performed with *Trimmomatic* [SE; LEADING Q25; TRAILING Q25; SLIDINGWINDOW 5:25; MINLEN 200]. Chimeras were identified using USEARCH61 and the GOLD database as suggested in the QIIME pipeline. After chimera were removed, sequences were clustered into Operational Taxonomic Units (OTU). Taxonomic classification was assigned to OTUs using the SILVA database (www.arb-silva.de/; version 119) with a cutoff of 97 % using the QIIME pipeline *pick_open_reference_otus.py* (11). Singletons, OTUs with an occurrence of less than 0.2 % in each sample, and chloroplasts were removed from subsequent analyses. Metagenome sequences are available at EMBL-EBI under accession number PRJEB20402 with the sample IDs ERS1666624-ERS1666714.

Statistical analyses. The OTUs shared between samples or unique for a specific sample set were identified using an online tool (http://bioinformatics.psb.ugent.be/webtools/Venn/). Multivariate statistics were done with PAST 3.17 (12).

Metaproteomics. Total crude biochemical extracts were prepared from 20 to 40 g of sample with GuHCl buffer (4 M guanidine-hydrochloride, 0.5 M EDTA, 0.5 M Tris pH 7.4) following the procedure described by Tuross and Stathoplos (13). Final extracts were re-suspended in sterile distilled water, dialyzed (>1200 Da cut off) against water, and finally lyophilized. The proteomic analysis was performed in the Proteomics Unit of Universidad Complutense de Madrid (UCM), Spain. Samples were cleaned and concentrated in a stacking gel (4 % SDS), then the band containing all proteins was stained with Coomassie Blue and cut from the gel to carry out in gel trypsin digestion. Then, tryptic peptides were analyzed by liquid chromatography and mass spectrometry, the masses assigned to peptide sequences, and the protein identified (14). Additionally, crude soil extracts were tested for the presence of preserved universal proteins by a multiplex microarray immunoassay as described (15).

Cultivation. To stimulate the growth of viable cells 15 g of sediment samples were transferred to a 50 mL conical tube and sparsely moistened with sterile water. The screw cap was loosely closed and the tube was incubated in a horizontal position at 28^{o}C for 3 days. During this period samples were moistened once a day. The sample was then transferred to a 500 mL screw cap flask and mixed with 4 mL NaCl (0.9 %, wt/vol) and 1 mL TSA Medium (1/10 strength) and incubated overnight at 28^{o}C on an orbital shaker (120 rpm). Dilutions in NaCl (0.9 %, wt/vol) were plated on different media (see below) depending on the predominant ionic concentrations characteristic to the given sample site and depth or on halophile enrichment media with different NaCl concentrations. All plates were incubated at 28^{o}C.

Media. For the cultivation, the following media were chosen (the recipes are given for 1 liter medium). Enrichment medium for moderate halophiles (EMH-2 %): 20 g NaCl, 20 g $MgSO_4 \times 7$ H_2O, 3 g Na-citrate, 7.5 g casaminoacids, 1 g yeast extract, 5 g tryptone, 0.05 g $Fe(NH_4)2(SO_4)2 \times 6$ H_2O, 0.5 g K_2HPO_4, pH 7.8; enrichment medium for halophiles to extreme halophiles (EH-5 %, EH-12.5 %, EH-25 %): 50/125/250 g NaCl, 2 g KCl, 20 g $MgSO_4 \times 7$ H_2O, 0.023 g $FeCl_3$, 3 g Na-citrate, 5 g casaminoacids, 5 g yeast extract, pH 7.8; sample site characteristic medium for AL 0-5 cm (AL-Na/Ca): 15 g NaCl, 3.764 g $CaSO_4 \times 2$ H_2O, 0.75 g KNO_3, 2 g $MgCl_2 \times 6$ H_2O, 0.05 g $FeSO_4 \times 7$ H_2O, 1 g TSA; pH 6.9; ssc medium for YU 0-5/20-30 cm (YU-Ca): 26 g $CaSO_4 \times 2$ H_2O, 0.112 g KNO_3, 0.25 g $MgCl_2 \times 6$ H_2O, 0.05 g $FeSO_4 \times 7$ H_2O, 1 g TSA; pH 7.6; ssc medium for YU 50/100 cm (YU-Na): 90 g Na_2SO_4, 9 g $MgCl_2 \times 6$ H_2O, 8.2 g $Ca(NO_3)_4$, 13.3 g $CaSO_4 \times 2$ H_2O, 2.16 g KNO_3, 0.05 g $FeSO_4 \times 7$ H_2O, 1 g TSA, pH 8.0. All media were solidified with 20 g agar and supplemented with cycloheximide (10 μg/mL) to avoid the growth of fungi.

Phylogenetic analysis of the isolates. Purified isolates were used for PCR amplification with bacterial 16S rRNA gene primers 27F and 907R (16). PCR products were sequenced (GATC, Konstanz, Germany) and the partial 16S rDNA sequences were compared by BLAST (17) to known sequences in GenBank (www.ncbi.nlm.nih.gov).

Fluorescein diacetate hydrolytic activity. Fluorescein diacetate (FDA) is a colorless nonpolar compound that penetrates cell membranes by passive diffusion and is hydrolyzed intracellularly by a number of enzymes, such as proteases, lipases, and esterases which are produced by metabolically active microorganisms (18, 19). The product is fluorescein, which can be measured in a fluorometer with an excitation/emission setting around 485/520 nm. FDA hydrolytic activity was determined following the protocol of Green *et al.* (20). Briefly, 4 g of sediment was mixed with 10 mL sterile potassium phosphate buffer (60 mM, pH 7.6) and 0.25 mL of 4.9 mL FDA dissolved in acetone, and incubated at 37^{o}C for 3 h on an orbital shaker (100 rpm). Enzyme reactions were terminated by the addition of 0.6 mL acetone. 1 mL of the sediment slurry was transferred to a 1.5 mL reaction tube and centrifuged (8800 g, 5 min). The fluorescence intensity of the supernatant was measured in a microplate reader (Clariostar, BMG LABTECH, Germany). End point concentrations were calculated from a standard curve with sodium fluorescein.

Phospholipids/Phospholipid Fatty Acids Analysis (PLFA).

Extraction and column separation. Approximately 60 to 90 g of freeze-dried ground samples were extracted by using a flow blending system with a 200 mL mixture of methanol/dichloromethane/ammonium acetate buffer (2:1:0.8, pH 7.6) modified after Bligh and Dyer (21). The solvent extract was transferred into a separation funnel for phase separation. As internal standards, 50 μg of 1-myristyl-(D27)-2-hydroxy-sn-glycerol-3-phosphocholine was added. For phase separation dichloromethane and water were added to achieve a ratio of 1:1:0.9 of methanol/dichloromethane/ammonium acetate buffer mixture and the organic phase was removed. The water phase was re-extracted twice with dichloromethane and all organic phases were combined. Subsequently, the obtained sediment extract was separated into four fractions of different polarity (low polar lipids, free fatty acids, glycolipids, and phospholipids (PLs)). Two columns were used in sequence. The upper column was filled with 1 g silica gel (63 to 200 μm) and topped with 0.5 g of sodium sulfate. The lower column was filled with 1 g Florisil. According to the method described by Zink and Mangelsdorf (22), the low polar fraction was eluted with 20 mL of chloroform, the free fatty acids with 50 mL of methyl formiate blended with 12.5 μL of glacial acetic acid and the glycolipid fraction with 20 mL of acetone. After removal of the Florisil column the PLs were eluted with 25 mL of methanol from the silica column. To improve the recovery of PLs, the silica column was rinsed with 25 mL of a methanol/water mixture (60:40) and the extract was captured in a separation funnel. 15 mL of dichloromethane and 3.5 mL of water were added for phase separation (methanol/dichloromethane/water, 1:1:0.9), the organic phase was removed, and the water phase was re-extracted twice with dichloromethane. Finally, the organic phases were combined and all fractions were evaporated to dryness and stored at -20^oC until analysis.

Detection of Phospholipid Fatty Acids (PLFAs). After sediment extraction and column separation, one half of the PL fraction was used for PLFA analysis following fatty acid cleavage procedures (23). Subsequently, the resulting PLFAs were measured by gas chromatography-mass spectrometry (GC-MS). The GC-MS measurements were conducted on a Trace GC Ultra (Thermo Electron Corporation) coupled to a DSQ Thermo Finnigan Quadrupole MS (Thermo Electron Corporation). The GC was equipped with a cold injection system operating in the splitless mode and a SGE BPX 5 fused-silica capillary column (50 m length, 0.22 mm ID, 0.25 μm film thickness) using the following temperature conditions: initial temperature 50^{o}C (1 min isothermal), heating rate 3^{o}C/min to 310^{o}C, held isothermally for 30 min. Helium was used as carrier gas with a constant flow of 1 mL/min. The injector temperature was programmed from 50 to 300^{o}C at a rate of 10^{o}C/s. The MS operated in the electron impact mode at 70 eV. Full-scan mass spectra were recorded from m/z 50 - 650 at a scan rate of 1.5 scans/s.

Calculation of cell load per g sediment. Total amounts of PLFAs in pmole per gram sediment dry weight were multiplied by 20,000 cells/pmol following a conversion factor presented by Balkwill *et al.* (24).

ATP Analyses. Sediment samples were placed in a sterile autoclave bag and crushed to smaller pieces (up to a maximum diameter of approximately 1 cm) using a hammer. Six grams of sediment or crushed rock samples were introduced into a 50 mL centrifuge tube, and 5 mL of ice-cold sodium phosphate buffer (0.12 M Na_2HPO_4, NaH_2PO_4, pH = 8.0) were added. Samples were shaken on an orbital shaker for 5 min at 150 rpm, cooled on ice for 3 min, and shaken again for another 5 min. Samples were then centrifuged at 4^{o}C and 500 g for 10 min. The supernatants containing the dislodged cells as well as extracellular ATP (eATP) were recovered in a 15 mL centrifuge tube, and 1 mL of sodium phosphate buffer was added to the sediment samples. Above procedure was repeated 3 times and supernatants were collected. The collected suspensions were centrifuged at 4^{o}C and 4,600 g for 60 min. Supernatants containing the eATP fraction were recovered in 15 mL centrifuge tubes. Cell pellets containing intracellular ATP (iATP) were re-suspended in 1-4 mL of sodium phosphate buffer and the particles in the solution were allowed to settle for approximately 30 min before samples were subjected to ATP analysis. All samples were processed in triplicates. ATP was quantified using the luciferase-based BacTiter-GloTM Microbial Cell Viability Assay (Promega). Measurements were carried out in opaque 1.5 mL microcentrifuge tubes according to the manufacturer's protocol, using a 6-point calibration curve with ATP concentrations ranging from 10 pM to 1 μM. The sample solutions containing iATP or eATP, respectively, were measured undiluted. 0.12 M sodium phosphate buffer was used as a blank and for diluting the standard series. 100 μL of sample solution, blank, or standard were mixed with 100 μL of BacTiter-GloTM reagent, which was prepared on the day before measurement and kept at room temperature until measurements were performed. Five minutes after mixing, luminescence was recorded using a Glomax 20/20 luminometer (Promega). All samples were analyzed in duplicates. ATP concentrations were normalized to sample weight.

Read-based metagenomics, genome-resolved metagenomics, and *in situ* replication rates. Metagenomic DNA was extracted from 10 g of soil mixed in 40 mL of cell extraction buffer (1 % PEG-8000, 1M NaCl, pH 9.2) as described before (25). The suspension was centrifuged at 44000 g for 2 h at 4^{o}C. Subsequently, DNA was extracted from the pellet using bead beating and a phenol-chloroform-isoamylalcohol (PCI) protocol (25, 26). To obtain sufficient DNA for sequence library construction, DNA from three extractions were combined. DNA was sheared with Covaris system targeting 500 bp fragments. Metagenomic libraries were constructed using NEBNext Ultra DNA Library Prep Kit for Illumina and NEBNext Multiplex Oligos for Illumina. Purification and size selection was done with Agencourt AMPure XP (aimed for the approximate insert size 500-700 bp). DNA size and concentration was evaluated with Fragment Analyzer^{TM} and PicoGreen method. Negative extractions controls yielded DNA concentrations below PicoGreen detection level. Finally, sequencing was done as paired-end sequencing (2×300 bp) on an Illumina MiSeq system. Negative extraction controls using the same procedure revealed 100-fold fewer reads and analysis of the generated reads revealed that they were taxonomically distinct from those obtained from the soil samples. For downstream analysis, adapters were removed and low quality sequences were identified and removed using Adapterremova v2.1.7 (27). Coverage of the metagenomics datasets was evaluated using Nonpareil v2.4 with default settings (28). Taxonomic classification was done with Kaiju using option greedy-5 (29). Microbial, viral, fungi and microbial eukaryotic genomes were downloaded from NCBI 18.01.2017. PCA plot was done with taxonomical data at the level of order, if possible. PCA plot additionally had a 5 % relative abundances cut-off, which was made in R using the r-package VEGAN (30). Metagenome sequences are available at GenBank/EMBL under BioProject ID PRJNA395196.

Metagenomic reads assigned to viruses which name contained host information and reads of their respective host were extracted. Abundance expressed in percentage of viruses and bacterial host were correlated using the *rcorr* function (Spearman rho rank correlation) from the package Hmisc v4.0-3 in R v3.3.1. Ranks were computed using efficient algorithms and midranks for ties. The asymptotic P-values are reported.

Genome resolved-metagenomics was performed for samples from the Yungay and Maria Elena site as outlined in Fig. 3. In brief, quality filtered MiSeq reads (https://sourceforge.net/projects/bbmap/, https://github.com/najoshi/sickle) were assembled using metaSPADES (31) and genes were predicted (32) for scaffolds greater than 1 kb. Taxonomic predictions of scaffolds were performed using a consensus of taxonomy of predicted proteins searched (33) against UniRef100 (34). Coverage of scaffolds was calculated using bowtie2 mapping (default settings) (35). Genomes were binned using tetranucleotide frequency-based emergent self-organizing maps (36) as described previously (37). Binned genomes were curated for scaffolding errors using ra2 (38) and underwent an additional binning step using GC, coverage and taxonomy of scaffolds. Final bins were used for completeness estimation based the presence of on 51 bacterial single copy genes (37) and used for calculating *in situ* genome replication rates (iRep) allowing a maximum of three mismatches per mapped read (39). Rank abundance curves were calculated based on ribosomal protein S3 (rpS3), which were retrieved from annotation against UniRef100 (34). Abundance was calculated for the entire scaffolding carrying the rpS3 gene as described above.

Metabolites.

Soil extraction. About 5 g of soil were extracted in purified water (MilliQ-Integral, Merck KGaA, Darmstadt, Germany) by ice-cold ultrasonication for 30 minutes. Supernatants were removed after centrifugation for 10 minutes at 4^{o}C and acidified to pH 2 with hydrochloric acid (32 %, p.a., Merck KGaA, Darmstadt, Germany) before passing them through Bond Elut PPL 100 mg (Agilent Technologies, Waldbronn, Germany) solid phase extraction (SPE) cartridges with a constant flow rate of <5 mL min^{-1}. The cartridges were rinsed with acidified (pH 2) purified water and dried under vacuum before eluting them with 1 mL of methanol (Chromasolv LC-MS grade methanol, Sigma Aldrich, Taufkirchen, Germany). The eluate was kept at −20^{o}C for further analysis.

ESI(-) FT-ICR-MS analysis. Mass spectra were acquired in negative ionization mode using a SolariX Qe FT-ICR-MS equipped with a 12 T superconducting magnet and coupled to an Apollo II electrospray ionization source (Bruker Daltonik, Bremen, Germany). Methanolic extracts were diluted 1:20 with methanol and continuously infused with a flow rate of 120 μL h^{-1}. Spectra accumulated 500 scans within a mass range of 147 to 1000 m/z. An internal calibration was performed with a mass accuracy of <0.1 ppm and peaks with a signal to noise ration >4 were picked. Formula assignment was performed with an in-house written software (NetCalc) using a network approach to calculate chemical compositions containing carbon, hydrogen and oxygen, as well as nitrogen and/or sulfur (40). The mass accuracy window for the formula assignment was set to ±0.5 ppm and the assigned formulas were validated by setting sensible chemical constraints (N rule; O/C ratio $\geq$ 1; H/C ratio $\leq$ 2n+2 (C_nH_{n+2}), double bond equivalents) in conjunction with isotope pattern comparison. Results were visualized by the use of van Krevelen diagrams in which the hydrogen to carbon ratio (H/C) was plotted against the oxygen to carbon ratio (O/C). The different bubble sizes represent the intensity of the characteristic molecular formula within the respective sample.

Fungal Analyses.

Fungal biomass. Fungal biomass was determined by using ergosterol as fungal biomarker (41). A protocol developed for plant litter (42) was adapted to account for the extremely low fungal biomass associated with desert soils. The soil samples were weighed in batches of 50 g and placed in 50 mL Falcon tubes. Grains >2 mm were removed. Addition of 18 mL of methanol/KOH (8 g/L) resulted in complete submergence of the soil. Ergosterol and ergosterol esters were extracted and saponified in the sealed tubes by placing them into a water bath at 80^{o}C for 40 min. Extraction efficiency was improved by vortexing the tubes about every 8 min. Subsequently, the supernatants were transferred to clean Falcon tubes and the soil rinsed three times with 4 mL of methanol. The combined supernatants were acidified with 0.65 M HCl, then loaded onto an SPE column (Waters Sep-Pak®, Vac RC, tC18, 500 mg sorbent) as described in Gessner (43). The sorbent bed of

the column was washed and dried under a stream of air at 16°C to prevent ergosterol losses, before eluting the sterol with isopropanol and further concentrating the solution to a final volume of up to 200 μL. Final separation and quantification of ergosterol was achieved by reversed-phase chromatography (Lichrospher RP18 column; (43) using a 100 μL injection loop). The limits of detection and quantification were determined by injecting 12 ergosterol standards (ACROS Organics; $\geq$98 % purity) dissolved in isopropanol at a concentration of 1 μg/mL, corresponding to an ergosterol content of 1 ng/g of the initial dry soil sample.

Fungal diversity. Total genomic DNA was extracted from 5-6 g of soil per sample depending on soil type using a phenol-chloroform-isoamylalcohol (PCI) bead beating protocol modified after Nercessian *et al.* (44). To improve DNA precipitation 1 μL linear polyacrylamide was added during the precipitation step. Sequencing of two fungal markers covering the ITS2 and the D2 region of the 28S rRNA gene was done as paired-end sequencing (2×300 bp) on an Illumina MiSeq system at LGC Genomics (Berlin, Germany) using the primer pairs ITS3mix-ITS4ngs (45) and LR22R-LR3 (46), respectively. Utilization of two fungal markers allowed to compare possible taxonomic overlaps and differences created by the different markers. Sequences were quality checked and analyzed using Mothur v1.37.6 (47). Sequences shorter than 250 bp or which contained ambiguities or homopolymer stretches of more than 8 bases were removed. Chimera check was performed using UCHIME. Sequences were clustered into operational taxonomic units (OTU) using VSEARCH (48) as implemented in Mothur with a sequence similarity of $\geq$97 %. OTUs represented by only a singleton sequence were removed. Taxonomy assignment of the OTUs was done with the RDP Online Classifier (49) using the WARCUP Fungal ITS set for ITS sequences and the SINA Online Classifier v1.2.11 (50) for LSU sequences, based on Silva database v128, with a confidence threshold of 60 %.

Endospore quantification. Dipicolinic acid (DPA) was extracted following Fichtel *et al.* (51) with slight modifications. For each sample, two subsamples of about 1 g were prepared. To the first subsample 2 mL of a Tris buffer solution (0.2 M, pH = 7.6) was added, while for the second sample the extraction solution was spiked with pure DPA (Sigma Aldrich) to a final concentration of 200 nM. Both subsamples were extracted through autoclaving (121°C, 20 min). 40 μL aluminium chloride (2 mM) was added afterwards to aid precipitation of phosphates that could potentially interfere with fluorescence detection. After centrifugation (3,500 rpm, 5 minutes) the supernatants were filtered (Chromafil cellulose acetate filter 0.2 μm) and stored at -20^{o} C until analysis. Before analysis, the extracts were acidified by addition of 20 % $NaHSO_4$ (500 mM) to ensure proper retention of DPA during chromatographic separation. Given the low concentrations observed in the investigated samples, an aliquot of the samples was concentrated by evaporation under a gentle stream of nitrogen, resuspended in $NaHSO_4$ (500 mM) and also analyzed. Chromatographic separation of DPA was achieved using a protocol with sodium bisulfate (50 mM, pH = 1.2) and acetonitrile as mobile phases (52). Slight modifications included the use of a reversed phase column with smaller particle size and inner diameter (Phenomenex Gemini 3 μm C_{18} 150 × 2 mm). Terbium chloride (50 μM) was added post-column solved in 1 M sodium ccetate (pH $\sim$ 9). This post-column approach guarantees both good chromatographic separation at acidic conditions and efficient complexation of Tb and DPA, as this complex requires higher pHs to remain stable and offer optimal fluorescence (53). Detection of the Tb-DPA complex was achieved with a Thermo FLD-3400RS by targeting the characteristic emission maximum at 543 nm after excitation at 271 nm. The built-in filter wheel of the FLD-3400RS was used to suppress stray light and higher order effects. Otherwise, excitation at 271 nm and emission at about twice this wavelength would be strongly affected by second order effects. DPA concentrations were converted into endospore concentrations per g of soil with an average cellular DPA concentration of 2.24×10^{-16} mol per endospore (51).

1. France-Lanord C, Sheppard S (1992) *Hydrogen isotope composition of pore waters and interlayer water in sediments from the central western Pacific, Leg 129*.
2. Craddock PR, Dauphas N (2011) Iron Isotopic Compositions of Geological Reference Materials and Chondrites. *Geostandards and Geoanalytical Research* 35:101–123.
3. Mulder I, et al. (2013) A new purge and trap headspace technique to analyze low volatile compounds from fluid inclusions of rocks and minerals. *Chemical Geology* 358:148–155.
4. Greule M, Mosandl A, Hamilton JTG, Keppler F (2008) A rapid and precise method for determination of D/H ratios of plant methoxyl groups. *Rapid Communications in Mass Spectrometry* 22:3983–3988.
5. Alawi M, Schneider B, Kallmeyer J (2014) A procedure for separate recovery of extra- and intracellular DNA from a single marine sediment sample. *Journal of Microbiological Methods* 104:36–42.
6. Holben WE, Jansson JK, Chelm BK, Tiedje JM (1988) DNA probe method for the detection of specific microorganisms in the soil bacterial community. *Appl. Environ. Microbiol.* 54:703–711.
7. Ogram A, Sayler GS, Barkay T (1987) The extraction and purification of microbial DNA from sediments. *Journal of Microbiological Methods* 7:57–66.
8. Nadkarni M, Martin FE, Jacques NA, Hunter N (2002) Determination of bacterial load by real-time PCR using a broad range (universal) probe and primer set. *Microbiology* 148:257–266.
9. Martin M (2011) Cutadapt removes adapter sequences from high-throughput sequencing reads. *EMBnet.journal* 17:10.
10. Zhang J, Kobert K, Flouri T (2014) PEAR: A fast and accurate Illumina Paired-End reAd mergeR. *Bioinformatics* 30:614–620.
11. Caporaso JG, et al. (2010) QIIME allows analysis of high-throughput community sequencing data. *Nature methods* 7:335–336.
12. Hammer Y, Harper DAT, Ryan PD (2001) Paleontological Statistics Software: Package for Education and Data Analysis. *Palaeontologia Electronica* 4:9.
13. Tuross N, Stathoplos L (1993) *Ancient Proteins in Fossil Bones.* Vol. 224, pp. 121–129.
14. Gil-Bona A, et al. (2015) *Candida albicans* cell shaving uncovers new proteins involved in cell wall integrity, yeast to hypha transition, stress response and host-pathogen interaction. *Journal of Proteomics* 127:340–351.
15. Parro V, et al. (2011) A microbial oasis in the hypersaline atacama subsurface discovered by a life detector chip: implications for the search for life on mars. *Astrobiology* 11:969–96.
16. Lane DJ (1991) 16S/23S rRNA sequencing in *Nucleic Acid Techniques in Bacterial Systematics*, eds. Stackebrandt E, Goodfellow M. pp. 115–175.
17. Altschul S, Gish W, Miller W, Myers E, Lipman D (1990) Basic Local Alignment Search Tool. *J. Mol. Biol.* pp. 403–410.
18. Chrzanowski TH, Crotty RD, Hubbard JG, Welch RP (1984) Applicability of the fluorescein diacetate method of detecting active bacteria in freshwater. *Microbial Ecology* 10:179–185.
19. Chand S, Lusunzi I, Veal DA, Williams LR, Karuso P (1994) Rapid screening of the antimicrobial activity of extracts and natural products. *The Journal of antibiotics* 47:1295–1304.
20. Green VS, Stott DE, Diack M (2006) Assay for fluorescein diacetate hydrolytic activity: Optimization for soil samples. *Soil Biology and Biochemistry* 38:693–701.
21. Bligh EG, Dyer WJ (1959) A rapid method of total lipid extraction and purification. *Canadian Journal of Biochemistry and Physiology* 37:911–917.
22. Zink KG, Mangelsdorf K (2004) Efficient and rapid method for extraction of intact phospholipids from sediments combined with molecular structure elucidation using LC-ESI-MS-MS analysis. *Analytical and Bioanalytical Chemistry* 380:798–812.
23. Müller KD, Husmann H, Nalik HP (1990) A new and rapid method for the assay of bacterial fatty acids using high resolution capillary gas chromatography and trimethylsulfonium hydroxide. *Zentralblatt Für Bakteriologie: International Journal of Medical Microbiology* 274:174–182.
24. Balkwill DL, Leach FR, Wilson JT, McNabb JF, White DC (1988) Equivalence of microbial biomass measures based on membrane lipid and cell wall components, adenosine triphosphate, and direct counts in subsurface aquifer sediments. *Microbial Ecology* 16:73–84.
25. Narayan A, Jain K, Shah AR, Madamwar D (2016) An efficient and cost-effective method for DNA extraction from athalassohaline soil using a newly formulated cell extraction buffer. *3 Biotech* 6:1–7.
26. Töwe S, et al. (2011) Improved protocol for the simultaneous extraction and column-based separation of DNA and RNA from different soils. *Journal of Microbiological Methods* 84:406–412.
27. Schubert M, Lindgreen S, Orlando L (2016) AdapterRemoval v2: rapid adapter trimming, identification, and read merging. *BMC Research Notes* 9:88.

28. Rodriguez-R LM, Konstantinidis KT (2014) Nonpareil: A redundancy-based approach to assess the level of coverage in metagenomic datasets. *Bioinformatics* 30:629–635.
29. Menzel P, Ng KL, Krogh A (2016) Fast and sensitive taxonomic classification for metagenomics with Kaiju. *Nature Communications* 7:11257.
30. Dixon P (2003) VEGAN, a package of R functions for community ecology. *Journal of Vegetation Science* 14:927.
31. Nurk S, Meleshko D, Korobeynikov A, Pevzner PA (2017) metaSPAdes: a new versatile metagenomic assembler. *Genome research* 27:824–834.
32. Hyatt D, et al. (2010) Prodigal: prokaryotic gene recognition and translation initiation site identification. *BMC bioinformatics* 11:119.
33. Buchfink B, Xie C, Huson DH (2015) Fast and sensitive protein alignment using DIAMOND. *Nature methods* 12:59–60.
34. Suzek BE, Huang H, McGarvey P, Mazumder R, Wu CH (2007) UniRef: comprehensive and non-redundant UniProt reference clusters. *Bioinformatics (Oxford, England)* 23:1282–1288.
35. Langmead B, Salzberg SL (2012) Fast gapped-read alignment with Bowtie 2. *Nature methods* 9:357–359.
36. Dick GJ, et al. (2009) Community-wide analysis of microbial genome sequence signatures. *Genome biology* 10:R85.
37. Probst AJ, et al. (2016) Genomic resolution of a cold subsurface aquifer community provides metabolic insights for novel microbes adapted to high CO2 concentrations. *Environmental Microbiology* 19:459–474.
38. Brown CT, et al. (2015) Unusual biology across a group comprising more than 15% of domain Bacteria. *Nature* 523:208–211.
39. Brown CT, Olm MR, Thomas BC, Banfield JF (2016) Measurement of bacterial replication rates in microbial communities. *Nature Biotechnology* 34:1256–1263.
40. Tziotis D, Hertkorn N, Schmitt-Kopplin P (2011) Letter: Kendrick-analogous network visualisation of ion cyclotron resonance Fourier transform mass spectra: improved options for the assignment of elemental compositions and the classification of organic molecular complexity. *European Journal of Mass Spectrometry* 17:415.
41. Gessner MO, Newell SY (2002) *Biomass, growth rate, and production of filamentous fungi in plant litter.* (Washington, DC, USA: ASM Press) Vol. 2, pp. 390–408.
42. Gessner MO, Schmitt AL (1996) Use of solid-phase extraction to determine ergosterol concentrations in plant tissue colonized by fungi. *Applied and Environmental Microbiology* 62:415–419.
43. Gessner MO (2005) Ergosterol as a measure of fungal biomass in *Methods to Study Litter Decomposition: A Practical Guide*. pp. 189–195.
44. Nercessian O, Noyes E, Kalyuzhnaya MG, Lidstrom ME, Chistoserdova L (2005) Bacterial populations active in metabolism of C1 compounds in the sediment of Lake Washington, a freshwater lake. *Applied and Environmental Microbiology* 71:6885–6899.
45. Tedersoo L, et al. (2014) Global diversity and geography of soil fungi. *Science* 346:1256688–1256688.
46. Mueller RC, Gallegos-Graves LV, Kuske CR (2016) A new fungal large subunit ribosomal RNA primer for high-throughput sequencing surveys. *FEMS Microbiology Ecology* 92:1–11.
47. Schloss PD, et al. (2009) Introducing mothur: Open-source, platform-independent, community-supported software for describing and comparing microbial communities. *Applied and Environmental Microbiology* 75:7537–7541.
48. Rognes T, Flouri T, Nichols B, Quince C, Mahé F (2016) VSEARCH: a versatile open source tool for metagenomics. *PeerJ* 4:E2584.
49. Wang Q, Garrity GM, Tiedje JM, Cole JR (2007) Native Bayesian classifier for rapid assignment of rRNA sequences into the new bacterial taxonomy. *Applied and Environmental Microbiology* 73:5261–5267.
50. Pruesse E, Peplies J, Glöckner FO (2012) SINA: Accurate high-throughput multiple sequence alignment of ribosomal RNA genes. *Bioinformatics* 28:1823–1829.
51. Fichtel J, Köster J, Scholz-Böttcher B, Sass H, Rullkötter J (2007) A highly sensitive HPLC method for determination of nanomolar concentrations of dipicolinic acid, a characteristic constituent of bacterial endospores. *Journal of Microbiological Methods* 70:319–327.
52. Fichtel J, Köster J, Rullkötter J, Sass H (2007) Spore dipicolinic acid contents used for estimating the number of endospores in sediments. *FEMS Microbiology Ecology* 61:522–532.
53. Hindle AA, Hall EA (1999) Dipicolinic acid (DPA) assay revisited and appraised for spore detection. *The Analyst* 124:1599–604.
54. Bozkurt D, Rondanelli R, Garreaud R, Arriagada A (2016) Impact of Warmer Eastern Tropical Pacific SST on the March 2015 Atacama Floods. *Monthly Weather Review* 144:4441–4460.
55. Gonçalves VN, et al. (2016) Fungi associated with rocks of the Atacama Desert: Taxonomy, distribution, diversity, ecology and bioprospection for bioactive compounds. *Environmental Microbiology* 18:232–245.
56. Rubio MC, Runco R, Navarro AR (2002) Invertase from a strain of *Rhodotorula glutinis*. *Phytochemistry* 61:605–609.
57. Montes MJ, et al. (1999) Polyphasic taxonomy of a novel yeast isolated from antarctic environment; Description of *Cryptococcus victoriae* sp. nov. *Systematic and Applied Microbiology* 22:97–105.
58. Gazquez F, Evans NP, Hodell DA (2017) Precise and accurate isotope fractionation factors (α17O, α18O and αD) for water and CaSO4·2H2O (gypsum). *Geochimica et Cosmochimica Acta* 198:259–270.
59. Ewing SA, et al. (2008) Non-biological fractionation of stable Ca isotopes in soils of the Atacama Desert, Chile. *Geochimica et Cosmochimica Acta* 72:1096–1110.

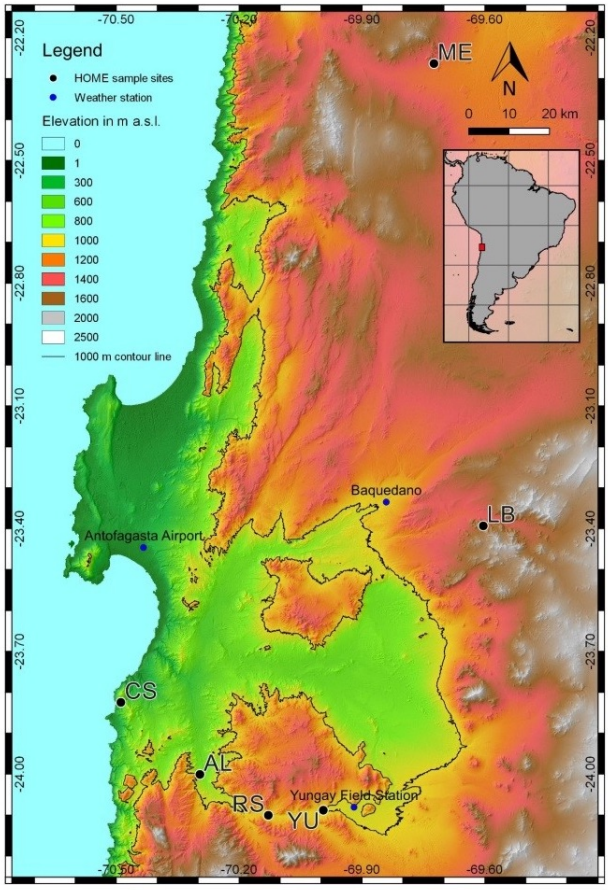

Fig. S1. Map of sampling site locations and rain gauge stations (for site descriptions see Material and Methods Section).

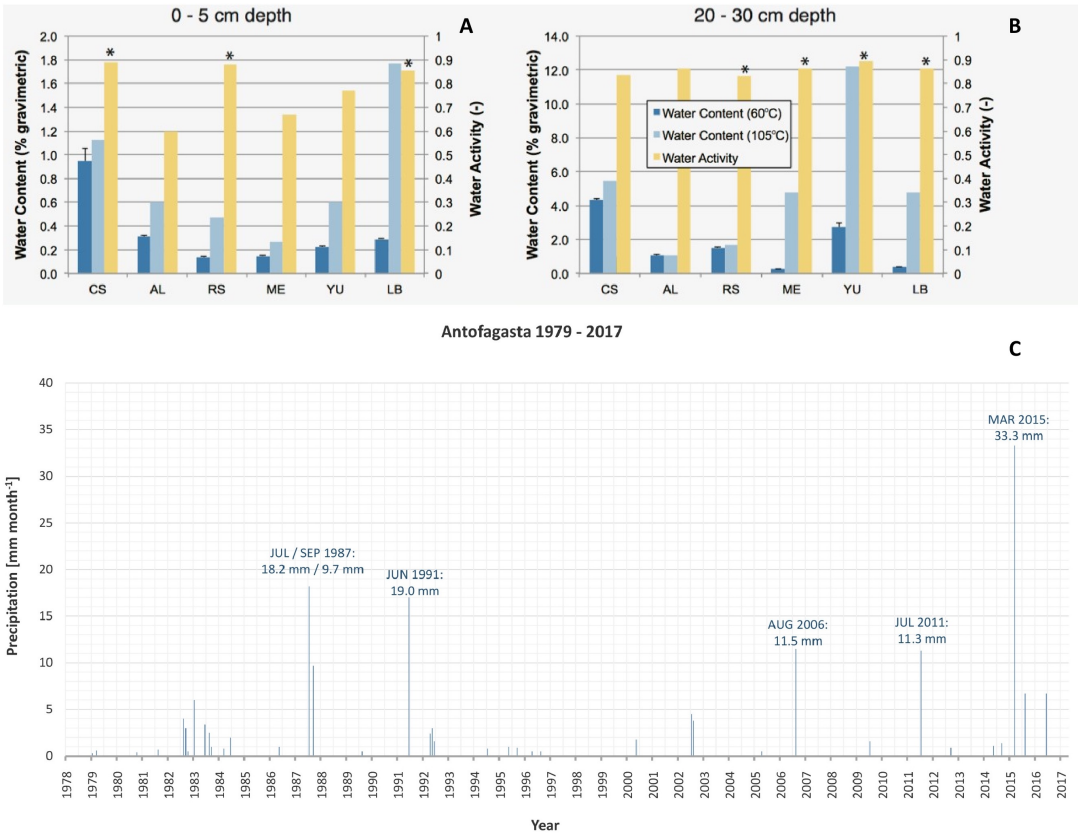

Fig. S2. A, B. Water contents (% gravimetric) determined by drying at 60^{o}C and 105^{o}C and water activities of soil samples (depth 0-5 cm and 20-30 cm) from coastal to inland sites on April 21-28, 2015. Water activities were determined from the moisture sorption isotherms and the water contents measured at 105^{o}C. The difference in measured water content at 60^{o}C and 105^{o}C for samples containing gypsum (ME (20-30cm); YU (0-5 and 20-30 cm)) is in part a result of released crystal water from gypsum when heated to the higher temperature, an effect also noticed in the sample preparation for XRD analysis, in which all of the original gypsum was dehydrated to bassanite when heated to 105^{o}C. Stars on top of water activity indicates that the measured water activity was the maximum possible with the instrument, so that the true water activity is larger than this value. **C. Monthly rainfall totals (mm) at Antofagasta Rain Gauge (Altitude: 50 m, Latitude S 23^{o} 35' 51", Longitude W 70^{o} 23' 12"), with dates given of highest precipitation totals.** All precipitation recorded at the Antofagasta airport station in spring 2015 fell in the period of March 24-26 in 2015, as a result of a cutoff low off the coast of northern Chile and positive sea surface temperature anomalies over the eastern tropical Pacific, which favored the unusual atmospheric conditions (54).

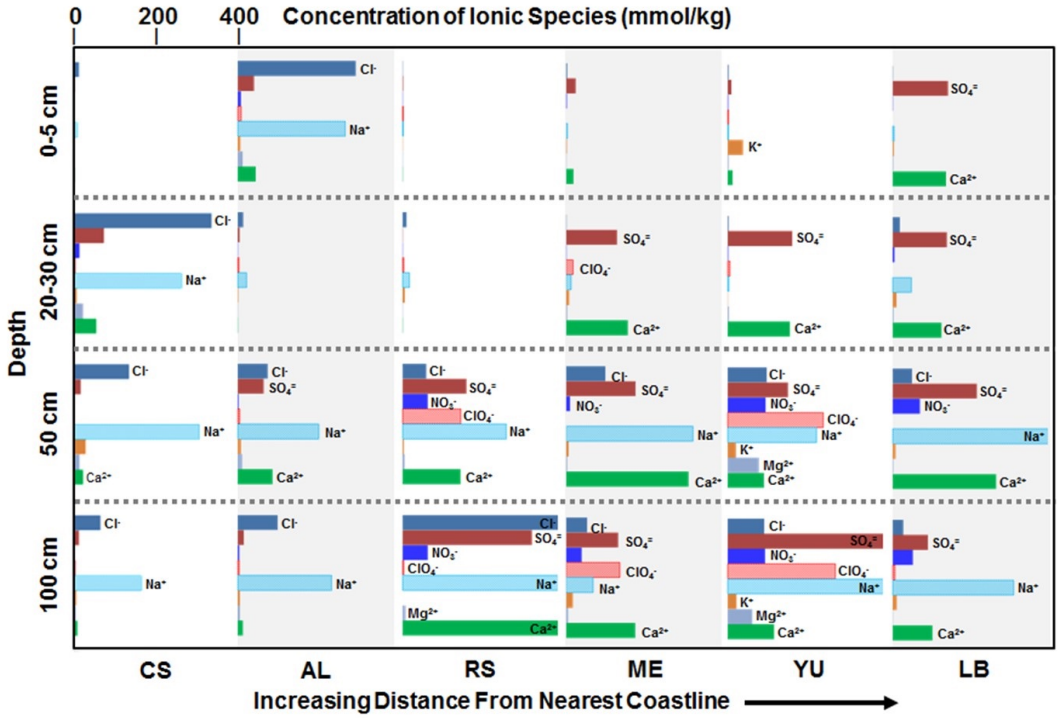

Fig. S3. Concentration of soluble salt anions and cations as a function of distance along the aridity gradient and depth.

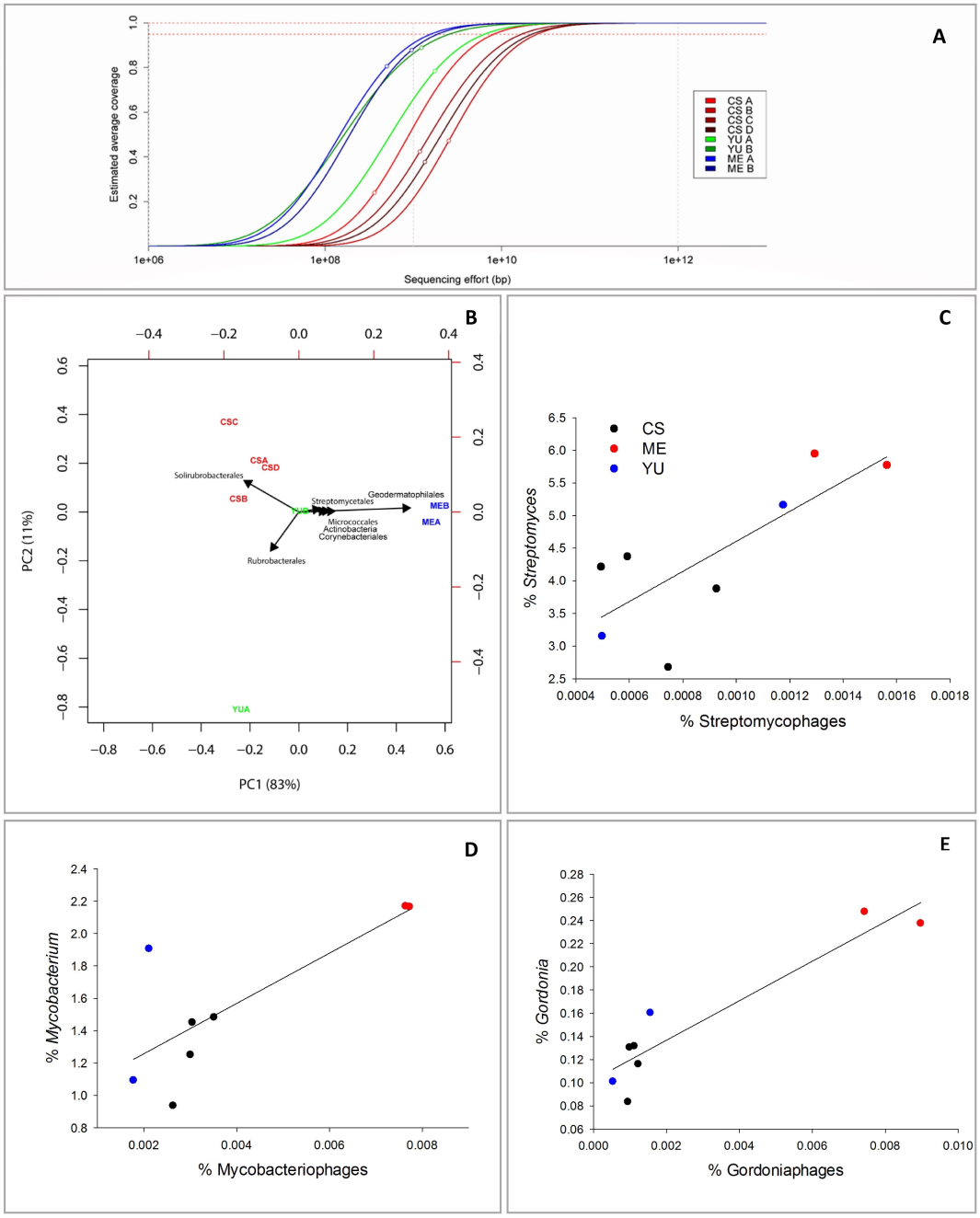

Fig. S4. Metagenomics results, A: Curves representing metagenome complexity of CS, YU, and ME. Circles represent the estimated coverage of the sample. Leftmost curves indicate lower diversity. **B. Phylogenetic principal component analysis of bacterial community composition using metagenomic read counts to describe the community structure in Coastal Soil (CS), Yungay (YU), and Maria Elena (ME)**. Biplots of the response orders were overlaid on the PCA plots as vectors. Most interestingly, the bacterial community composition of the two hyperarid areas ME and YU differs significantly, indicating a selection again indicating biological activity at least one of the two sites. **C,D,E: Abundance of mycobacteriophages, gordoniaphages and streptomycophages** correlated positively with the abundance of the respectively hosts found in the different samples with Spearman coefficient correlations $\rho = 0.69$ (probability = 0.058) $\rho = 0.88$ (probability = 0.003) and $\rho = 0.67$ (probability = 0.071), respectively.

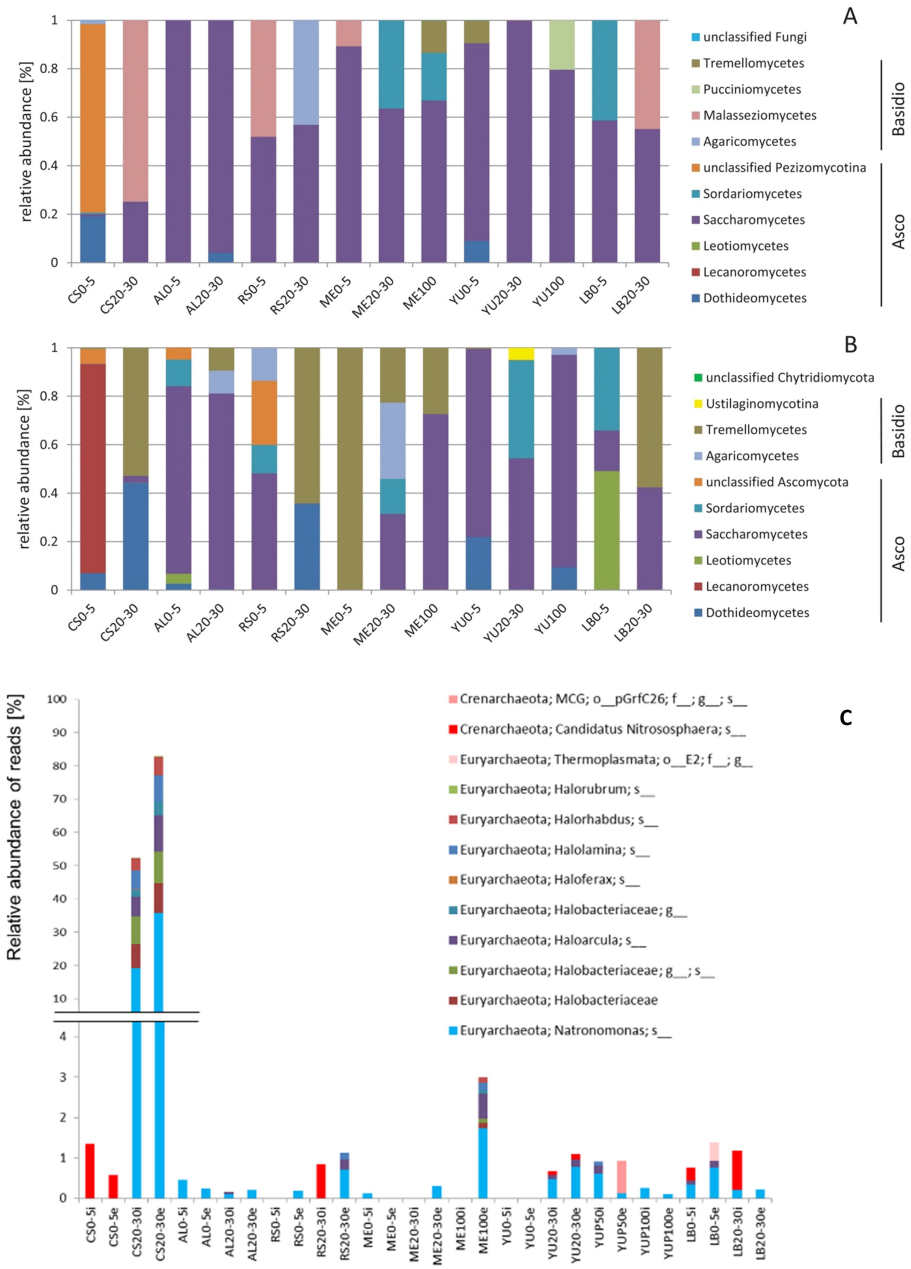

Fig. S5. A and B: Fungal taxonomic composition and relative abundance (in %) for all Atacama samples based on sequences of large ribosomal subunit (LSU, A) and internal transcribed spacer (ITS, B) gene marker. For B, sample ME 0-5 is only represented by a very low number of sequence reads and is therefore not representative. Asco – *Ascomycota*, Basidio – *Basidiomycota*. Altogether, 131 and 74 operational taxonomic units (OTU) for fungal LSU and ITS gene marker sequences, respectively, could be detected. Almost all OTUs belonged to *Asco-* and *Basidiomycota*, except OUT 42 (ITS) in sample CS 0-5 that was related to *Rhizophlyctis sp.*, belonged to the phylum *Chytridiomycota*. This group are fungal parasites that can grow for example on cyanobacteria which were detected in the surface sample of CS (e.g., 0-5 cm, see also Fig. S7). Many of the OTUs were related to fungal groups that have been isolated from extreme habitats (e.g. rock surfaces, hypersaline soils, Atacama Desert, Antarctica), such as *Acarospora sp.*, *Cladosporium sp.*, *Vishniacozyma sp.*, *Tausonia sp.* and *Teratosphaeria* (55–57). As we cannot exclude the deposition of fungal spores by wind to the investigated sites, it is possible that we have also detected dormant fungal life stages, especially since we were using molecular methods based on DNA amplification. Nevertheless, as we were able to detect OTUs that belong to known extremo-tolerant species, we conclude that fungi can proliferate under certain favorable conditions which might occur from time to time. Additionally, the detection of an OTU belonging to Chytridiomycota in the fog-influenced (CS) soil surface sample shows the potential of an active fungal parasitic infection life cycle in connection with cyanobacteria. **C: Relative abundances of archaeal taxa in the intracellular and extracellular DNA pools (i for intracellular, e for extracellular)**. Notice the predominance of *Archaea* (mostly *Halobacteria*) in the subsurface layer at CS.

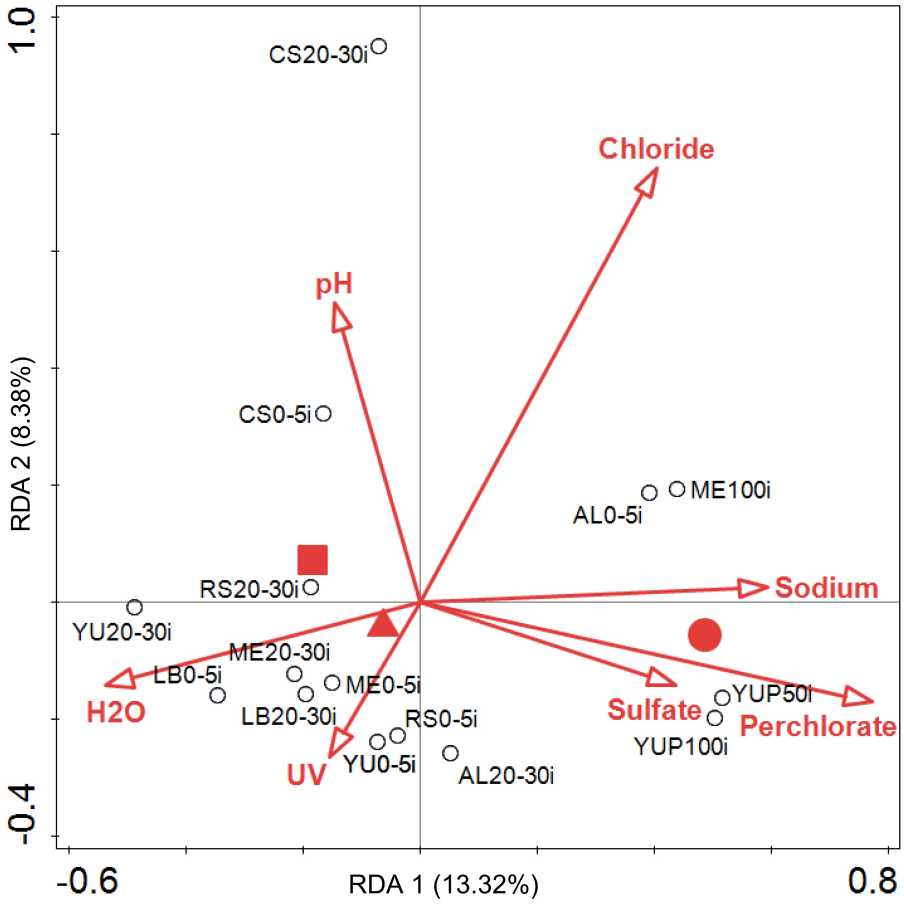

Fig. S6. RDA analysis of the OTU abundances in the iDNA pools from the sites CS, AL, RS, YU, ME and LB. The data were Chord transformed to make them applicable for the linear method. The vectors represent the environmental parameters with the strongest effects on the community composition. The symbols indicate the three depths (triangle, surface 0-5 cm; square, subsurface 20-30 cm; circle, deeper subsurface, 50-100 cm). Multivariate statistics were done with Canoco 5.0 (www.canoco5.com).

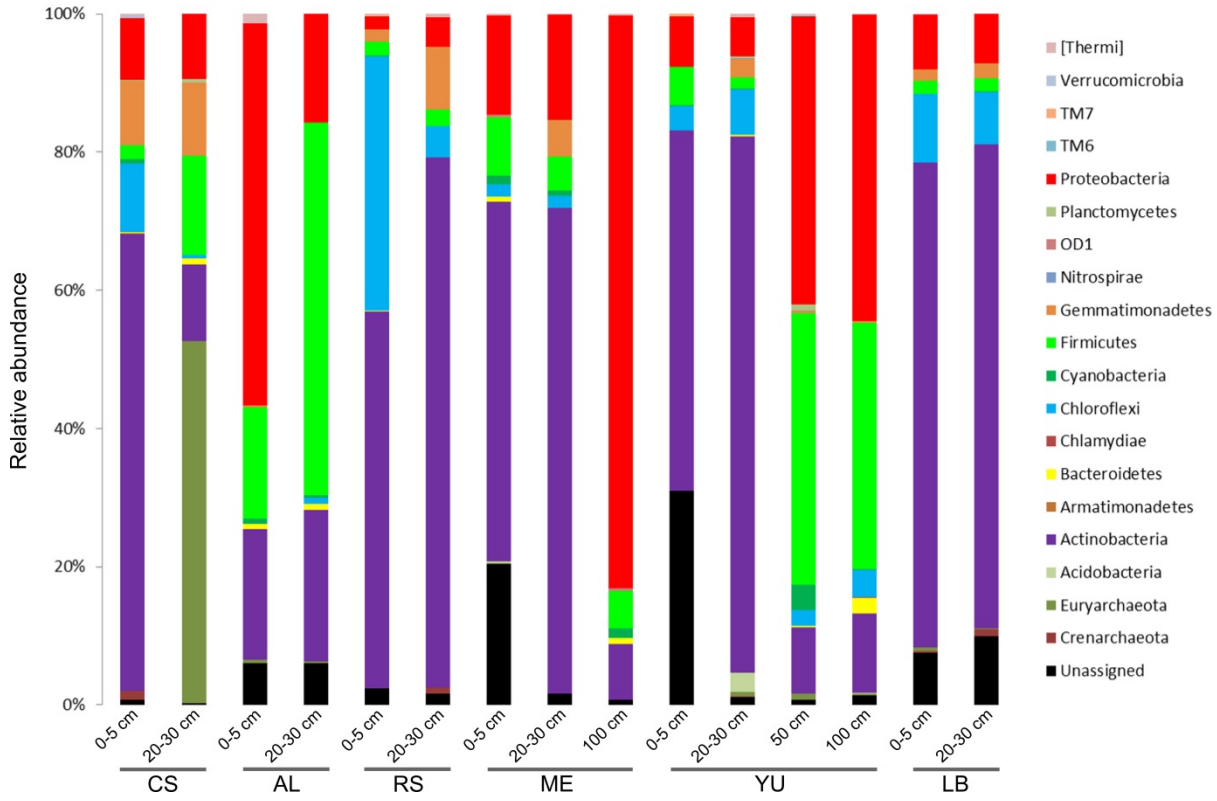

Fig. S7. Relative abundances of microbial phyla in iDNA pools of the six sampling sites Coastal Soil (CS), Alluvial Fan (AL), Red Sands (RS), Maria Elena (ME), Yungay (YU), and Lomas Bayas (LB) for the sampling depths 0-5 cm, 20-30 cm, 50 cm, and 100 cm. Results from merged triplicates.

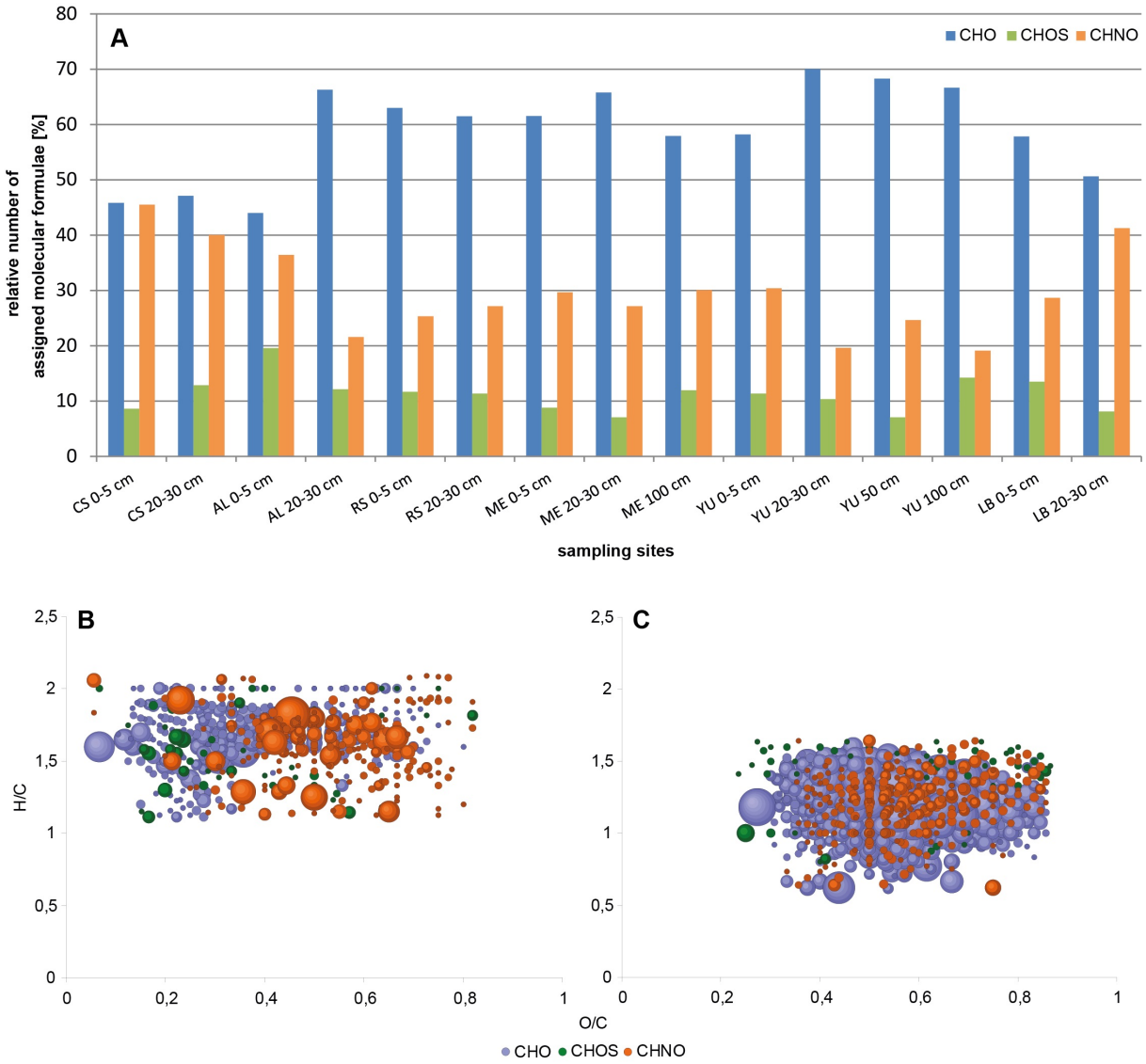

Fig. S8. (**A**) Relative abundances of assigned molecular formulae for soil organic matter collected at different sites in the Atacama Desert and at different soil depths. Elemental compositions are plotted as CHO (blue), CHOS (green) and CHNO (orange). (**B-C**) Van Krevelen diagrams of selected molecular formulae at the YU and ME sampling sites, decreasing and increasing with depth, respectively. (**B**) The enhanced presence of fatty acids, amino acids and small peptides indicates metabolic activity in the upper soil horizons (0-5 and 20-30 cm) at the YU and ME sites. (**C**) For the 50-100 cm YU and ME sites, assigned masses with higher intensities represent signals that correlate with a geochemical signature and with regular chemical patterns in the CHO and CHNO elemental compositions. See Fig. S9A for comparison.

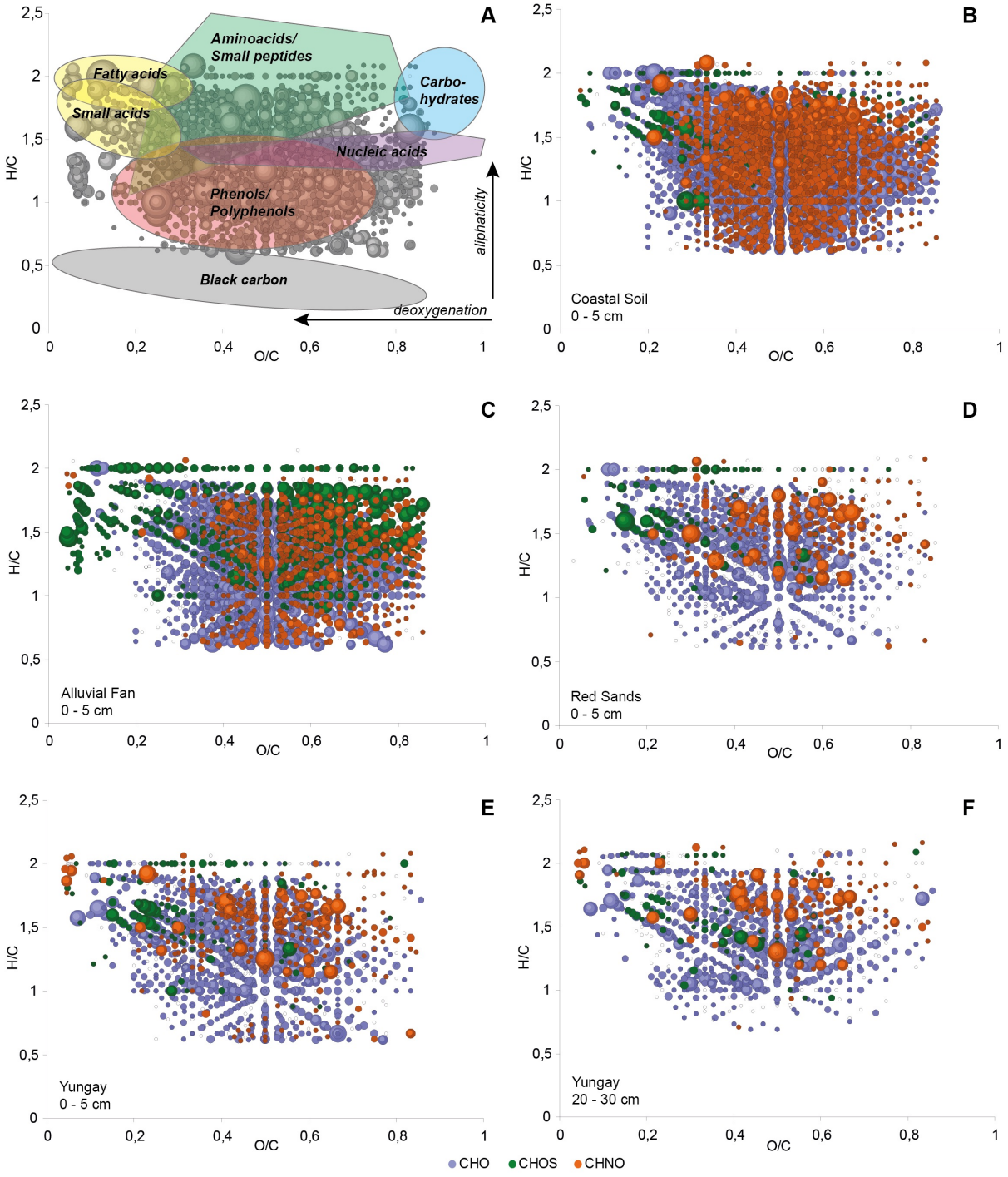

Fig. S9. Positions of chemical classes (colored areas) are depicted in compositional space of a van Krevelen diagram according to their hydrogen to carbon (H/C) versus oxygen to carbon (O/C) ratios (A). Elemental compositions are plotted as CHO (blue), CHOS (green) and CHNO (orange) and bubble sizes depict mass signal intensities. Highly aliphatic compounds are mostly presented in the upper area (H/C ratio $>$ 1), whereas PAHs are found within the oxidized black carbon zone (H/C ration $<$ 0.6). Van Krevelen diagrams of assigned molecular formulae of surface extracts from sampling sites Coastal Soil, Alluvial Fan, Red Sands and Yungay (B-E) show a large decrease in abundance of sulfur and nitrogen containing molecular compositions along the gradient from coast to the hyperarid area in the Atacama Desert. Depicted results confirm the presence of metabolic transformation products like fatty acids or amino acids and indicate biological activity. Comparing van Krevelen diagrams E and F compositional abundances slightly decrease with increasing depth at Yungay. The wide distribution within the compositional space reflects the complexity of the samples from amino acids to small peptides to phenolic compounds supporting a specific level of bioactivity in the hyperarid region.

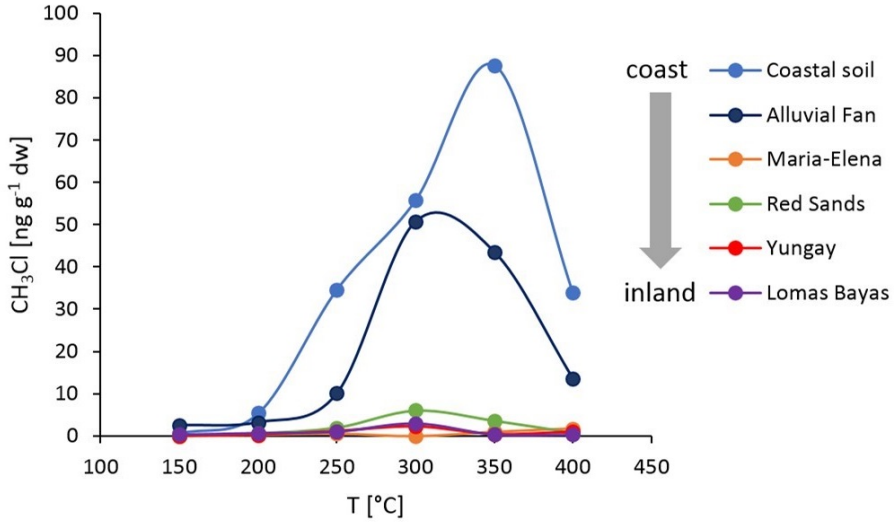

Fig. S10. Low Temperature Pyrolysis (150 to 400°C) of Atacama surface soils shows very distinct chloromethane production profiles for the six regions, with the maximum at CS (Coastal Soil) and the minimum at LB (Lomas Bayas) and Maria Elena (ME).

Table S1. i/eDNA and i/eATP values for the years 2015 to 2017. 16S gene copy numbers g^{-1} of sediment with universal bacterial primers 331F – 797R in intracellular (i) and extracellular (e) DNA pools as well as ATP concentrations (mol) g^{-1} of sediment in intracellular (iATP) and extracellular (eATP) ATP pools. Numbers in parentheses indicate the SD values. n = 3.

Year		2015		2016		2017	
Depth [cm]		0 – 5	20 – 30	0 – 5	20 - 30	0 - 5	20 - 30
CS	iDNA	6.1 x 10^5 (±4.9 x 10^5)	2.3 x 10^5 (±4.3 x 10^4)	n.s.	n.s.	9.7 x 10^1 (±1.2 x 10^2)	0 *
	eDNA	3.9 x 10^7 (±1.7 x 10^7)	6.5 x 10^5 (±3.5 x 10^5)	n.s.	n.s.	9.3 x 10^4 (±1.1 x 10^5)	1.1 x 10^4 (±4.0 x 10^3)
	iATP	3.1 x 10^{-12} (±2.6 x 10^{-12})	9.0 x 10^{-15}# (±5.0 x 10^{-15})	n.s.	n.s.	1.0 x 10^{-12} (±5.1 x 10^{-13})	5.1 x 10^{-14} (±3.3 x 10^{-14})
	eATP	3.0 x 10^{-12} (±9.5 x 10^{-13})	9.6 x 10^{-14} (±1,2x 10^{-14})	n.s.	n.s.	7.9 x 10^{-13} (±1.4 x 10^{-13})	8.4 x 10^{-15} (±5.3 x 10^{-15})
AL	iDNA	1.3 x 10^3 (±4.9 x 10^2)	5.8 x 10^3 (±2.9 x10^3)	n.s.	n.s.	0 *	7.0 x 10^1 (±5.2 x 10^1)
	eDNA	2.8 x 10^3 (±3.5 x 10^3)	1.2 x 10^4 (±1.6 x 10^4)	n.s.	n.s.	1.1 x 10^2 (±1.5 x 10^2)	0 *
	iATP	4.7 x 10^{-15}*# (±4.7 x 10^{-15})	n.s.	n.s.	n.s.	4.8 x 10^{-15} # (±7.3 x 10^{-16})	6.5 x 10^{-15} # (±9.9 x 10^{-16})
	eATP	9.9 x 10^{-15} (±3.7 x 10^{-15})	n.s.	n.s.	n.s.	3.4 x 10^{-15} # (±1.4 x 10^{-16})	3.43x 10^{-15} # (±7.4 x 10^{-16})
RS	iDNA	4.6 x 10^4 (±7.8 x 10^4)	1.1 x 10^6 (±2.5 x 10^5)	n.s.	n.s.	2.2 x 10^1 (±1.7 x 10^1)	0 *
	eDNA	7.0 x 10^4 (±7.9 x 10^4)	7.5 x 10^2 (±2.7 x 10^2)	n.s.	n.s.	1.3 x 10^2 (±7.9 x 10^1)	7.4 x 10^1 (±1.1 x 10^2)
	iATP	8.0 x 10^{-15} # (±2.7 x 10^{-15})	1.8 x 10^{-14} (±4.4 x 10^{-15})	n.s.	n.s.	2.3 x 10^{-15} (±1.4 x 10^{-15})	0 *
	eATP	1.8 x 10^{-14} (±3.1 x 10^{-15})	7.1 x 10^{-14} (±1.4 x 10^{-14})	n.s.	n.s.	3.0 x 10^{-15} # (±1.0 x 10^{-15})	1.8 x 10^{-14} (±2.9 x 10^{-14})
ME	iDNA	6.3 x 10^4 (±5.3 x 10^3)	8.6 x 10^3 (±4.1 x 10^3)	n.s.	n.s.	1.1 x 10^2 (±4.8 x 10^1)	5.6 x 10^1 (±2.0 x 10^1)
	eDNA	1.8 x 10^4 (±9.9 x 10^3)	8.3 x 10^1 (±1.2 x 10^2)	n.s.	n.s.	0 *	0 *
	iATP	n.s.	n.s.	n.s.	n.s.	0 *	0 *
	eATP	n.s.	n.s.	n.s.	n.s.	7.9 x 10^{-16} (±4.3 x 10^{-16})	0 *
YU	iDNA	1.0 x 10^4 (±3.3 x 10^2)	6.2 x 10^5 (±7.2 x 10^4)	3.1 x 10^2 (±2.1 x 10^2)	9.5 x 10^2 (±2.1 x 10^2)	4.2 x 10^1 (±3.6 x 10^1)	0 *
	eDNA	8.6 x 10^1 (±1.2 x 10^2)	1.9 x 10^4 (±3.4 x 10^3)	2.4 x 10^1 (±6.0 x 10^1)	2.2 x 10^2 (±5.3 x 10^1)	1.5 x 10^1 (±2.2 x 10^1)	0 *
	iATP	3.9 x 10^{-14} (±2.8 x 10^{-14})	1.8 x 10^{-14} (±4.2 x 10^{-15})	7.2 x 10^{-15} # (±3.3 x 10^{-15})	8.6 x 10^{-15} # (±5.1 x 10^{-15})	0 *	1.9 x 10^{-14} (±1.1 x 10^{-14})
	eATP	1.9 x 10^{-13} (±3.9 x 10^{-14})	4.4 x 10^{-13} (±4.1 x 10^{-14})	2.5 x 10^{-14} (±1.1 x 10^{-14})	1.5 x 10^{-14} (±1.7 x 10^{-14})	1.7 x 10^{-14} (±3.3 x 10^{-15})	3.0 x 10^{-14} (±3.8 x 10^{-15})
LB	iDNA	1.6 x 10^5 (±8.7 x 10^4)	7.4 x 10^4 (±3.7 x 10^4)	n.s.	n.s.	6.2 x 10^1 (±4.9 x 10^1)	2.0 x 10^2 (±1.0 x 10^2)
	eDNA	0 *	0 *	n.s.	n.s.	2.4 x 10^1 (±3.4 x 10^1)	1.2 x 10^2 (±9.8 x 10^1)
	iATP	n.s.	n.s.	n.s.	n.s.	3.2 x 10^{-15} # (±1.1 x 10^{-15})	0 *
	eATP	n.s.	n.s.	n.s.	n.s.	1.7 x 10^{-13} (±3.4 x 10^{-14})	0 *

n.s. = no sample; * = below the detection limit (DNA < 80 copies g^{-1}; ATP < 8.6 x 10^{-18} mol g^{-1}); # = below the qualification limit of ATP (< 2.8 x 10^{-15} mol g^{-1}).

Table S2. DPA-based endospore concentration (g^{-1}) for the stations and depths investigated during the 2015 sampling event. Concentrations are calculated by comparison to a spiked sample. Samples had to be concentrated after extraction except for stations CS and AL. Samples that needed to be concentrated could only be analyzed once. All other samples were analyzed in duplicate, with standard deviations ranging from 6 to 17 % of the average value. DPA concentration in YU 0-5 and 20-30cm and in LB 0-5 cm were at the detection limit of the employed method

Sample / depth	0-5 cm	20-30 cm	50 cm	100 cm
CS	7.74×10^5	2.78×10^6	N/A	N/A
AL	4.14×10^5	4.43×10^5	N/A	N/A
RS	1.62×10^4	2.41×10^4	N/A	N/A
ME	1.52×10^4	3.03×10^4	N/A	5.63×10^4
YU	$<7.18 \times 10^3$	$<9.31 \times 10^3$	2.62×10^5	1.66×10^5
LB	$<1.22 \times 10^4$	4.04×10^4	N/A	N/A

N/A = Not analyzed

Table S3. Sediment enzymatic activity as released fluorescein from fluorescein diacetate hydrolysation (nmol g^{-1} h^{-1}).

Depth (cm)	CS	AL	RS	ME	YU	LB
0 – 5	0.850	0.130	0.250	0.754	0.228	1.475
20 – 30	0.124	0.180	0.053	0.410	0.018	b.d.
50	-	-	-	-	b.d.	-
100	-	-	-	b.d.	b.d.	-

Notes: b. d., below detection limit of 0.001 nmol $g^{-1} \cdot h^{-1}$; for comparison freshly sampled garden soil showed an activity of 0.14 µmol $g^{-1} \cdot h^{-1}$

Table S4. Stable isotopic composition of hydrogen and oxygen of the water extracted from the studied soils. Based on the stoichiometric H_2O/S ratio for gypsum and the measured H_2O/S ratio almost all the extractable water from the YU samples is structural water from gypsum. The data implies an atmospheric origin of the water with different degrees of evaporation evidenced by negative and variable D_{excess} values, which inversely correlated with the moisture gradient along the sample sites. The YU 20-30 cm depth samples collected in 2015 (about one month after the rain event) and a year later in 2016 show drastically different isotope values indicating a lesser influence of evaporation in the 2015 samples. Together with recalculated isotopic compositions (58) of the pore water for the hyperarid locations this suggests that 1) extreme rain events at the hyperarid locations are isotopically fractionated by evaporation but partly re-equilibrate the gypsum in the subsurface, 2) most of the water at the hyperarid locations could be brought in as structural water of gypsum aerosols formed close to sea-salt-spray production, and 3) a downward motion of pore water. This percolation is also supported by the interpretation of the isotopic composition of sulfate (59). The close agreement between our $\delta^{34}S_{Sulfate}$ and $\delta^{18}O_{Sulfate}$ and the literature data, sampled a decade ago, implies a faster exchange of water than dissolved salt. Together with the re-equilibration (differences between YU samples from 2015 and 2016) this makes gypsum structural water possibly accessible to microorganisms.

		Soil extractable water						Bulk soil sample				Bulk Sulfate	
Sample	Depth (cm)	H_2O [%]	$\delta^{18}O$	2σ	δD	2σ	D_{excess}	$\delta^{56}Fe$	2σ	$\delta^{57}Fe$	2σ	$\delta^{34}S$	$\delta^{18}O$
CS	20-30	3.76	-3.40	0.04	-24.9	1.1	2						
AL	0-5	1.14	-2.07	0.01	-31.7	0.4	-15	0.08	0.12	0.11	0.17	2.7	6.0
RS	0-5	-	-	-	-	-	-	0.01	0.04	0.00	0.09	-	-
RS	20-30	1.35	-3.56	0.05	-40.3	0.8	-12	-	-	-	-	-	-
ME	0-5	-	-	-	-	-	-	-	-	-	-	4.5	6.4
ME	20-30	-	-	-	-	-	-	-	-	-	-	3.9	4.2
YU	0-5	0.70	-1.95	0.17	-46.5	1.0	-31	-	-	-	-	1.4	-
YU	20-30	3.62	-1.59	0.04	-35.1	0.4	-22	-	-	-	-	-	-
YU	50	-	-	-	-	-	-	-	-	-	-	4.6	-
YU	100	0.82	-5.43	0.10	-59.8	0.6	-16	0.26	0.07	0.39	0.16	4.7	5.9
LB	0-5	-	-	-	-	-	-	-	-	-	-	8.5	7.3
LB	20-30	-	-	-	-	-	-	-	-	-	-	7.9	6.4
YU-2016	20-30	3.95	-4.28	0.29	-76.0	0.5	-42	-	-	-	-	-	-

Note: Except YU-20-30-2016 all samples were taken during the field campaign in 2015.